REPORT DOCUMENTATION PAGE

Form Approved
OMB No. 0704-0188

1. REPORT DATE *(DD-MM-YYYY)*	2. REPORT TYPE	3. DATES COVERED *(From - To)*
04/01/2023	Final Technical Report	02/08/2019 to 04/30/2023

4. TITLE AND SUBTITLE
A Universal Hardware-In-Loop Platform for Hybrid AC/DC Microgrids

5a. CONTRACT NUMBER
N.A

5b. GRANT NUMBER
N62909-19-1-2037

5c. PROGRAM ELEMENT NUMBER
N.A

6. AUTHOR(S)
Asst Prof Amer. M. Y. M Ghias Assoc Prof Hoay Beng Gooi, Dr. Zhang Xinan, Dr. Binyu Xiong

5d. PROJECT NUMBER
N.A

5e. TASK NUMBER
N.A

5f. WORK UNIT NUMBER
N.A

7. PERFORMING ORGANIZATION NAME(S) AND ADDRESS(ES)
Nanyang Technological University, Singapore
50 Nantang Avenue
Singapore 639798
Republic of Singapore

8. PERFORMING ORGANIZATION REPORT NUMBER

9. SPONSORING/MONITORING AGENCY NAME(S) AND ADDRESS(ES)
Office of Naval Research Global Science & Technology
Boston Regional Office
495 Summer Street
Boston, MA 02210

10. SPONSOR/MONITOR'S ACRONYM(S)
ONR-G

11. SPONSOR/MONITOR'S REPORT NUMBER(S)

12. DISTRIBUTION/AVAILABILITY STATEMENT
Approved for Public Release; Distribution is Unlimited

13. SUPPLEMENTARY NOTES
None

14. ABSTRACT

Isolated hybrid microgrids have been developed to power a remote village/island and reduce the dependency on the existing local/regional grid. The hybrid AC/DC microgrids have gained significant attention due to their flexibility in integrating renewable energy sources and energy storage systems. Most hybrid AC/DC microgrids are designed to operate in both grid-connected and stand-alone modes. The hybrid AC/DC microgrid is generally equipped with distributed energy resources, power electronics devices, and local loads. The experimental platforms to validate new topology and control methods for the hybrid AC/DC microgrids are often expensive. This project aims to develop a universal hardware-in-loop platform to do an experimental study for the proposed hybrid AC/DC microgrids. The significant findings to achieve such objectives are (1) the universal hardware-in-the-loop platform development. (2) A multi-stack vanadium redox flow battery model considering electrolyte transfer delay. (3) Peak power estimation method of vanadium redox flow battery for solar-battery powered electric vehicle charging stations. (4) Microgrid control method based on virtual synchronous machines in islanded mode.

15. SUBJECT TERMS
Hybrid Microgrid, Hardware-in-Loop, Energy Storage, Renewable Energy, Electric Vehicle, Advance Control, Virtual Synchronous Machines

16. SECURITY CLASSIFICATION OF:			17. LIMITATION OF ABSTRACT	18. NUMBER OF PAGES	19a. NAME OF RESPONSIBLE PERSON
a. REPORT	b. ABSTRACT	c. THIS PAGE			Amer. M. Y. M Ghias
U	U	U	SAR	51	19b. TELEPHONE NUMBER *(Include area code)* +65 67905631

School of Electrical & Electronic Engineering Nanyang Technological University

Office of Naval Research Global Science & Technology

A Universal Hardware-In-Loop Platform for Hybrid AC/DC Microgrids

Final Year Progress Report

by Asst Prof Amer. M. Y. M Ghias, Assoc Prof Hoay Beng Gooi, Dr. Zhang Xinan, Dr. Binyu Xiong

10 April 2023
Nanyang Technological University
Singapore

Executive Summary

Isolated hybrid microgrids have been developed to power a remote village/island and reduce the dependency on the existing local/regional grid. The hybrid AC/DC microgrids have gained significant attention these days due to their flexibility to integrate renewable energy sources and energy storage systems. Most hybrid AC/DC microgrids are designed to operate in both grid-connected and stand-alone modes. The hybrid AC/DC microgrid is generally equipped with distributed energy resources, power electronics devices, and local loads. The experimental platforms to validate any new topology and control methods for the hybrid AC/DC microgrids are often expensive. This project aims to develop a universal hardware-in-loop platform to do an experimental study for the proposed hybrid AC/DC microgrids.

To achieve such objectives, this project is divided into four work packages. They are:
(1) Development of a universal hardware-in-loop platform for a hybrid AC/DC microgrid.
(2) Regulation and optimization for hybrid AC/DC microgrids based on a universal hardware-in-loop platform.
(3) Advanced power converter design for hybrid AC/DC microgrids.
(4) Improved virtual synchronous machine technologies for the hybrid AC/DC microgrids.

The results obtained in the fourth year in each work package are described in this report. The significant findings are listed as follows:
(1) Development of the universal hardware-in-the-loop platform.
(2) A multi-stack vanadium redox flow battery model considering electrolyte transfer delay.
(3) Peak power estimation method of vanadium redox flow battery for solar-battery powered electric vehicle charging stations.
(4) Microgrid control method based on virtual synchronous machines in islanded mode

Acronyms and Abbreviations

AVR	Automatic voltage regulator
CERL	Clean energy research lab
CHIL	Control-hardware-in-loop
EMPC	Economic model predictive control
EVs	Electric vehicles
HESS	Hybrid energy storage system
HIL	Hardware-in-loop
OCV	Open-circuit voltage
PHIL	Power-hardware-in-loop
PV	Photovoltaic
SOC	State of charge
RESs	Renewable energy sources
VRB	Vanadium redox flow battery
VSDG	Variable speed diesel generator
VSM	Virtual synchronous machine

Table of Contents

List of Figures

List of Tables

ONRG Yearly Progress Report

Address to:
Attn:

Project Award No.: N62909-19-1-2037	
Project Title: A Universal Hardware-In-Loop Platform for Hybrid AC/DC Microgrids	
Project Commencement Date: 08 Feb, 2019	**Project Completion Date**: 30 Apr, 2023
Host Institution: Nanyang Technological University	**Principal Investigator:** Asst Prof Amer. M. Y. M Ghias

Project Period

Yearly Progress Report for the period 16 June 2022 to 30 April 2023. (Part A)

Part A

1. Project Management and Execution

Update on the project management schedule – Planned versus Actual.

Proposed Project Plan	Year 1				Year 2				Year 3				Year 4			
	Q1	Q2	Q3	Q4	Q1	Q2	Q3	Q4	Q1	Q2	Q3	Q4	Q1	Q2	Q3	Q4
Purchase lab supplies, consumables & materials																
Software & equipment setup in the laboratory																
Recruitment of researchers (RFs, RAs & REs)																
Design & development of the proposed system																
Testing of the unit modules & the proposed systems																
Testing & validation of the proposed overall system																
Publications																
Write reports																

On 7 September 2022, Project was extended till 30 April 2023.

Original schedule as in Project Overview
Actual progress to-date

2. Key Project Indicators

The key project indicators are summaries in the financial year format as follows:

Key Project Indicators	Year 1	Year 2	Year 3	Year 4	Total
Papers published in international journals	0	1	1	-	**2**
	4	3	3	11	**21**
Papers published in international conferences	1	1	2	-	**4**
	1	1	2	3	**7**
PhD students trained	0	0	0	-	0
	0	1	1	0	**2**
MSc/MEng students trained	0	2	0	-	**2**
	0	2	0	0	**2**
BEng students trained	1	2	2	-	**5**
	11	2	2	9	**24**
Total number of Researchers, Scientists, and Engineers (RSE) involved in the project	2	2	2	-	**6**
	2	1	1	4	**8**
Joint programs/projects with prestigious international research organizations	0	0	0	-	**0**
	0	0	0	0	**0**
Joint programs/projects with local universities	0	0	0	-	**0**
	1	0	0	0	**1**
Invention Disclosures	0	0	0	-	**0**
	0	0	0	0	**0**
External awards for research at international level	0	0	0	-	**0**
	0	0	0	0	**0**
No. of R&D projects with industry cash funding	0	0	0	-	**0**
	0	0	0	0	**0**
Industry dollars received to fund R&D projects (S$'000)	0	0	0	-	**0**
	0	0	0	0	**0**

Original target

Actual progress to-date

3. Cost Summary

Please refer to SF425 - Federal Financial Report for more information.

4. Management Approaches

During the past execution period, the project achievements are summarized into four main scopes (I)-(IV). The principal investigators of the project, Assoc Prof Gooi Hoay Beng (till end Feb 2023) and Asst Prof Amer Ghias (Mar-Apr 2023) carried out the project's overall execution.

Scopes I and II are under work package one and two (WP1 and WP2). They are carried out by senior lecturer Dr. Zhang Xinan (Collaborator, University of Western Australia), Asst Prof Amer. M. Y. M Ghais (Co-PI) and Research Fellow, Dr. Ujjal Manandhar, of NTU. Scopes III and IV are under work package three and four (WP3 and WP4). Asst Prof Amer M. Y. M Ghais (Co-PI) and Dr Gooi supervised the works carried out by the researcher, Dr. Binyu Xiong, from NTU. The technical support is provided by CERL technical staff members Chia-Nge Tak Heng, and Victor

Tan Chee Hou. Each of these work scopes is explicitly described. The key findings and detailed experimental results are presented in this report.

Part B

1. Development of a Universal HIL Platform for Hybrid AC/DC Microgrid.

The achievements under this work scope are summarized as follows:

- A control-hardware-in-loop (CHIL) platform has been built using the OPAL-RT real-time (RT) simulators OP5600/OP5607 and dSPACE MicroLabBox controller.
- The power-hardware-in-loop (PHIL) platform test has been conducted using the OPAL-RT real-time simulators OP5600/OP5607 and Spitzenberger and Spies (S&S) power amplifier.
- The hybrid energy storage system (HESS) consists of a battery, and a supercapacitor is tested using the PHIL experiment in the Clean Energy Research Lab (CERL).
- A new three-level bi-directional DC-DC converter with an original control method for renewable energy sources (RESs) and HESS has been proposed.
- Enhanced energy management and control methods for isolated power systems with a diesel generator, renewable energy resources, and HESS are proposed. The proposed method is validated using the PHIL experiment platform.
- The PHIL experimental study of the variable speed diesel generator (VSDG) is performed. The PHIL experimental study is used to study the stability of the VSDG in isolated power system configuration.

1.1 Control Hardware-in-Loop Platform

The digital simulation platforms, hardware platforms, and field tests are mostly adopted as validation methods for implementing new technologies in microgrids. There are several limitations as well as advantages of these platforms. The digital simulation platforms that use mathematical models of the target systems may not be reliable because some components are usually inaccurate or unavailable. The hardware or field tests eliminate the problems of digital simulation platforms. However, it requires a long setup time, high cost, and application-specific design. These challenges obstruct the extensive utilization of the hardware or field test platforms. These hardware platforms are costly to maintain and difficult to reconfigure. They limit the possibility of conducting the study of the different microgrid scenarios.

To solve these issues, the CHIL platform has been developed based on the OPAL-RT real-time simulators (OP5600/OP5607) and dSPACE MicroLabBox controller (ML1202). The CHIL platform combines the advantages of digital simulation and an external controller. The OP5600 real-time digital simulator at CERL is installed with 12 Intel Xeon E5 processors with a frequency of 3.2 GHz. Therefore, it provides powerful computational and simulation capability and allows the implementation of a complex power system simulation in real time. Moreover, the OP5600 has 64 analog I/O ports

and 64 digital I/O ports for interfacing with other equipment. Another real-time digital simulator OP5607, which is equipped with the Xilinx Virtex-7™ FPGA, provides a powerful floating-point electric hardware solver (eHS). The eHS solver enables the real-time simulation of the FPGA. These two real-time digital simulators can communicate rapidly with each other via the small form-factor pluggable transceiver and PCI express Gen2x4 so that the hardware-in-loop (HIL) simulation capability of the HIL platform can be significantly improved using the combination of these two simulators.

The dSPACE MicroLabBox controller is a compact all-in-one controller, with a dual-core real-time processor with a frequency of 2 GHz and 100 channels of high-performance I/O ports, including ADC I/Os, DAC I/Os, and digital I/Os. These I/Os are embedded in the model library of Matlab/Simulink. Moreover, the MicroLabBox controller supports the customized graphical control panel, so that the control panel layout can be designed according to the requirement of the target system.

The schematic and photo of the CHIL platform in CERL are shown in Fig. 1(a) and Fig. 1(b), respectively. The target plant can be simulated in OP5600/OP5607 in real time. Then the status of the target plant can be sent to the MicroLabBox controller via the analog output port of the real-time simulator and its ADC input ports. The control method implemented in the MicroLabBox will generate the proper control actions and then send them back to the real- time simulator via the digital I/O of these two equipment setups. This CHIL platform has been adopted by researchers and students in various projects and helped them generate fruitful results. The presented CHIL platform is easy to reconfigure, as well as saves development time, and overall cost of the experiment.

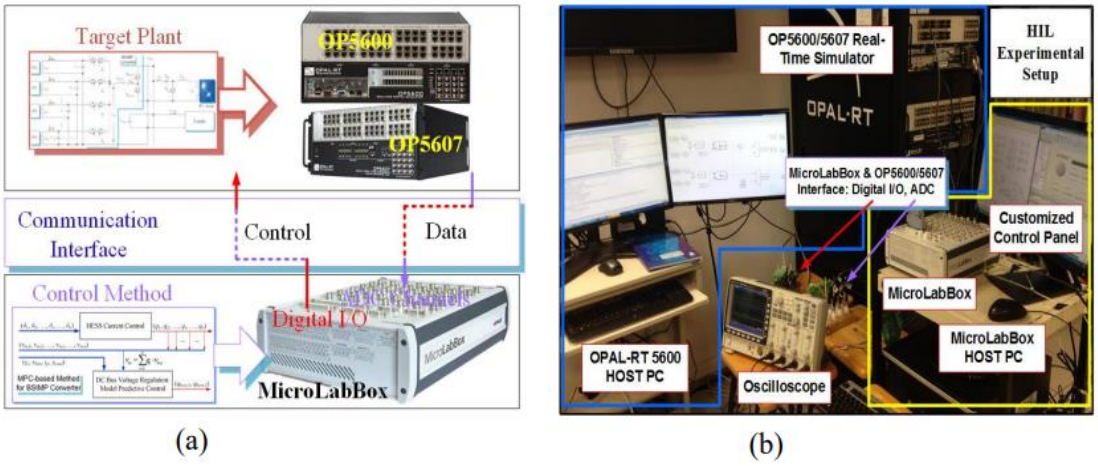

Fig. 1. HIL platform based on OP5600/OP5607 and MicroLabBox. (a) Schematic of CHIL platform. (b) Photo of CHIL platform.

1.2. Power Hardware-in-Loop Platform

To further extend the CHIL platform's capability, the power hardware-in-the-loop (PHIL) platform has been tested by combining the CHIL platform and the 45-kVA S&S power amplifier, as shown in Fig. 2(a). The PHIL platform enables the experiment of a complete system with one part simulated numerically and connected to real hardware

devices. The control methods are executed in the MicroLabBox controller. Simultaneously, the HESS and load are realized using the SAFT lithium-ion battery, GenPlus supercapacitor, and programmable load, and the remaining part of the microgrid is simulated in OP5600 and OP5607 real-time digital simulators. The three-phase 45-kVA S&S power amplifier is used as an interface between the CERL microgrid and the real-time digital simulator OP5600/OP5607. CERL at Nanyang Technological University, Singapore has a three-phase, 400-V (L-L), 50-Hz microgrid testbed to perform power system and power electronics studies. It comprises 2 x 18-kVA Chroma programmable AC source, 6-kVar capacitor bank, 5-kW solar photovoltaic (PV) system, 13.5-kW wind simulator, 2 x 10-kWh lithium-ion battery system, 15-kW supercapacitor system, 2 x 15-kVA Triphase PCS, 5-kW fuel cell system, 45-kVA power amplifier, 13.5-kW programmable load, 13.5-kVA synchronous generator, 215-kW Vycon flywheel system and 10-kW simulated industrial load. The microgrid is reconfigurable and can be operated in standalone mode or grid-connected mode. The CERL microgrid can also be used for the PHIL studies.

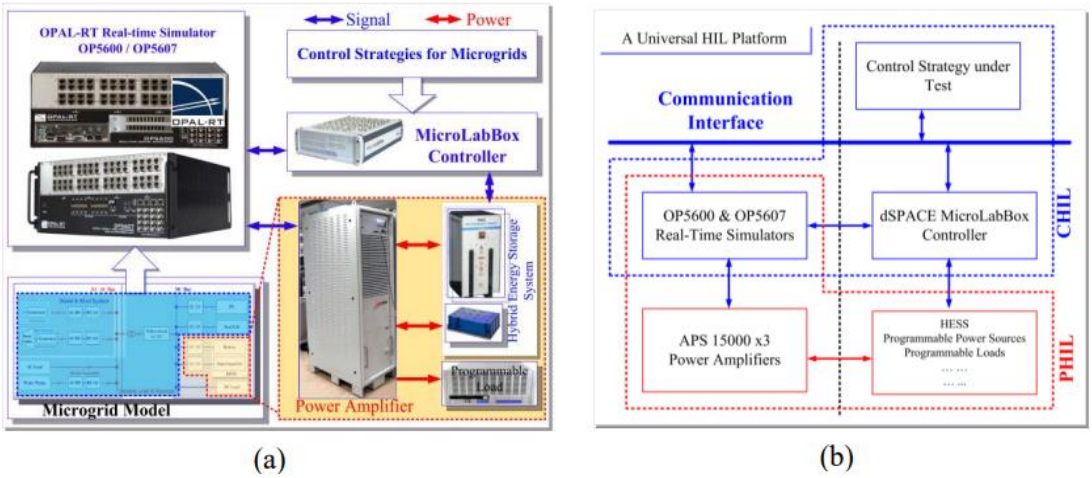

Fig. 2. Power hardware in the loop platform. (a) Representation of PHIL in CERL and (b) control and signal transfer architecture for PHIL.

2. A Multi-Stack Vanadium Redox Flow Battery Model Considering Electrolyte Transfer Delay

With the introduction of the “emission peak, and carbon neutral” target and the implementation of the green low-carbon energy development strategy, the construction of renewable-energy-based power systems has gained the top priority [1-2]. At the same time, To ensure power quality and improve the utilization rate of renewable energy, the scale of the corresponding energy storage systems is ever-increasing [3]. As a promising energy storage battery, the vanadium redox flow battery (VRB) has been widely investigated due to its high performance in terms of safety, independency in capacity and power design, dynamic response speed, and friendliness to the environment [4-6].

In hundred-kilowatt-scale energy storage projects, a single stack is often incapable of meeting the power and voltage needs. Many stacks are required to be series- and parallel-connected to achieve high voltage and high-power outputs. However, it has been found in applications that the capacity utilization and overall efficiency of a multi-stack VRB system are much lower than a VRB system with a single stack. It is obvious that apart from the performance of an individual stack, the overall performance of a large-scale VRB system is closely related to the stack connection layout. For single-stack cells, using high-performance electrode materials and appropriate electrolyte concentration can effectively increase the energy conversion efficiency of a single battery [7]. However, for multi-stack batteries, the transport of ions in the electrolyte inside of the pipe creates a shunt current between the cell and the stack [8]. To investigate the effect of the shunt current on the performance of the battery, Fink et al. [9] built a specific experimental setup for monitoring shunt currents between cells within a single stack. It was shown that the inner cells of a stack discharge faster than the outer ones. Wandschneider et al. [10] modelled the shunt current for a VRB system with three stacks. Chou et al. [11] developed a mathematical model based on Kirchhoff’s law to study the location and distribution of the shunt current within each stack and pipe. In addition to the shunt current, the ring current generated by the parallel connection of the stack also lowers the VRB capacity [12]. In particular, the different cell internal resistances of multiple stacks coupled with inappropriate series/parallel connections can significantly impact battery efficiency. In this regard, Chen et al. [13] developed a dynamic model to simulate the charging and discharging of eight stacks with different internal resistances under 35 different series and parallel layouts. Their results showed that the series connection of stacks with similar internal resistance could effectively improve the overall battery performance. Besides the electrical connection layout of the stack, the layout of the pipe is also a part to be considered. For example, König et al. [14] focused on the effect of pipe hydraulics on the performance of multi-stack systems, suggesting that using longer and narrower pipe designs can help reduce pumping losses and improve battery performance.

Most of the above studies focused on the effects of shunt current and losses due to different layouts on VRB performance. However, there has been no in-depth study on the effects of long-distance electrolyte delivery. Based on the effects of electrolyte delivery on the battery, this study firstly establishes a VRB dynamic model based on electrolyte transfer delay and builds a simulation model of six single-stack electrical series connections. The results show that, due to different electrolyte delivery distances of each stack, there is an electrolyte transfer delay phenomenon which can lead to different reactant concentrations in each stack. The inconsistent voltages of the stacks at the end of charging and discharging affect the battery's overall performance.

2.1 Multi-Stack Model Development

A single stack consists of a certain number of cells. The positive and negative electrolytes enter through the external liquid inlet and are distributed to the electrodes of each cell through the common flow channel to participate in the reaction. In practical engineering applications, depending on the power and voltage levels required, single stacks are connected in series and parallel via the common pipe to form multi-stack systems to meet the demand. To maximize the capacity of the multi-stack VRB system, it is necessary to ensure that the performances of stacks are highly consistent to prevent the "bucket effect" caused by the difference between stacks from affecting the overall performance of the battery. In this project, the voltage consistency of the individual stacks is used as a criterion for evaluation.

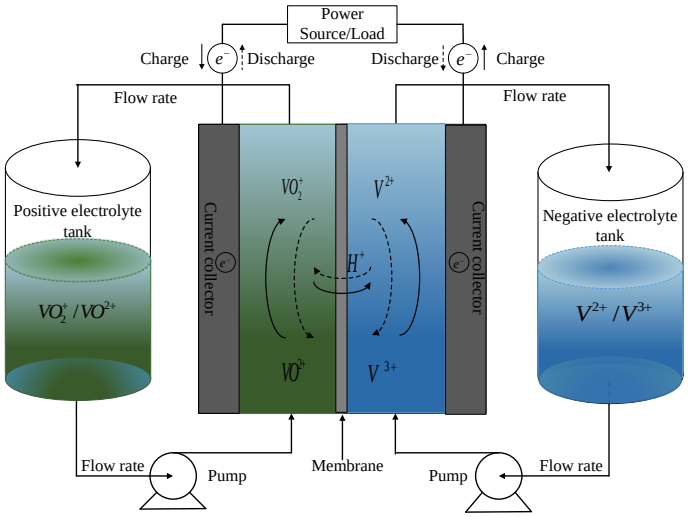

Fig. 3. VRB working principle.

A VRB generates electricity through the redox reaction of electrolytes on the surface of electrodes. As shown in Fig. 3, when the battery is running, the electrolyte in the positive and negative tanks is circularly transported to the battery flow channel through two pumps and pipe systems to participate in the chemical reactions and achieve energy conversion [15-16]. The relevant reactions are as follows:

Positive reaction equation:

$$VO^{2+} + H_2O \underset{\text{dischange}}{\overset{\text{change}}{\rightleftharpoons}} VO_2^+ + 2H^+ + e^- \quad (1)$$

Negative reaction equation:

$$V^{3+} + e^- \underset{\text{dischange}}{\overset{\text{change}}{\rightleftharpoons}} V^{2+} \quad (2)$$

Overall reaction equation:

$$VO^{2+} + V^{3+} + H_2O \underset{\text{dischange}}{\overset{\text{change}}{\rightleftharpoons}} VO_2^+ + V^{2+} + 2H^+ \quad (3)$$

2.1.1 Cell Voltage

For a stack, the stack voltage is the sum of the voltages of all cells. Assuming that the liquid flow within the stack is uniformly distributed and that all cells have the same performance given, the voltage of a single cell is calculated as:

$$E_{cell} = E_{ocv} + IR_{cell} + (\eta_{act} + \eta_{con}) \quad (4)$$

where E_{cell} denotes the cell voltage; E_{ocv} is the open-circuit voltage; *I* represents the current applied to the cell; R_{cell} denotes the equivalent resistance of the VRB cell; η_{act} is the activation overpotential of the cell; and η_{con} stands for the concentration overpotential of the cell. E_{ocv}, η_{act}, and η_{con} can be further expressed as [17-19]:

$$E_{ocv} = E_0 + \frac{RT}{zF} \ln\left(\frac{c_2^c c_5^c}{c_3^c c_4^c}\right) \quad (5)$$

$$\eta_{con} = \eta_{con}^+ + \eta_{con}^- = \frac{RT}{zF} \ln\left(1 - \frac{i}{zFk_m c_r^+}\right) + \frac{RT}{zF} \ln\left(1 - \frac{i}{zFk_m c_r^-}\right) \quad (6)$$

where E_0 denotes the standard potential of the overall reaction; R denotes the molar gas constant; T denotes the temperature of the VRB cell; F = 96,485 C/mol denotes the Faraday constant; and z = 1 denotes the unit activity coefficient. c_2^c, c_3^c, c_4^c and c_5^c denote the concentration of V^{2+}, V^{3+}, VO^{2+} and VO_2^+, respectively. c_r^+ and c_r^- denote the concentrations of the positive and negative reactions, respectively, which are presented in Table I. $k_m = 1.6 \times 10^{-4} \times \upsilon^{0.4}$ denotes the local mass transfer coefficient of the electrolyte [20], where υ denotes the velocity of the electrolyte. i represents the applied current density per electrode surface area.

Table I: Concentration c_r of the Active Species

c_r	Charge Mode	Discharge Mode
Positive electrode c_r^+	$c_{VO^{2+}}$	$c_{VO_2^+}$
Negative electrode c_r^-	$c_{V^{3+}}$	$c_{V^{2+}}$

As seen in (5) and (6), the reactant ion concentration affects the open-circuit voltage and concentration overpotential of the cell. In the following subsection, we will establish a dynamic model to describe the ion concentration.

2.1.2 Vanadium Ion Concentration Model

Based on the assumption that in VRB batteries, there is no transmigration of vanadium ions, and no self-discharge occurs, the vanadium ions in the tank and in the stack satisfy the following relationship based on the conservation of matter.

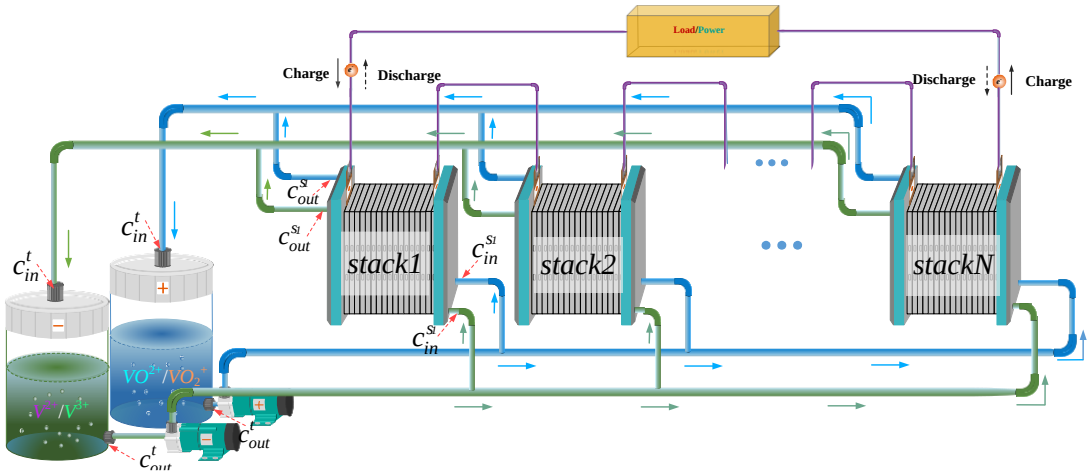

Fig. 4. A multi-stack VRB module.

First, in the tank, changes in vanadium ion concentration are mainly due to the flow of the electrolyte and can be described as

$$V_t \frac{dc_n^t(t)}{dt} = Q\left(c_n^s(t) - c_n^t(t)\right) \tag{7}$$

where V_t denotes the volume of the tank; c_n^t and c_n^s denote the concentration of the *n*th vanadium ion in the tank and stack, respectively; Q denotes the electrolyte flow rate. In the stack, changes in the vanadium ion concentration are related to electrochemical reactions and the flow of active species in the electrolyte. It can be expressed as

$$V_s \frac{dc_n^s(t)}{dt} = Q\left(c_n^t(t) - c_n^s(t)\right) \pm \frac{N_c I}{\mathrm{zF}} \tag{8}$$

where V_s denotes the volume of the stack and N_c denotes the number of cells in a stack.

For a multi-stack VRB module, as shown in Fig. 4, the electrolyte from the storage tanks is transferred through a common pipe to each stack, and according to the law of mass conservation, the vanadium ion substance concentrations in the stack and in the storage tank can be expressed as:

$$\begin{cases} V_s \dfrac{dc_{n,i}^s(t)}{dt} = Q\left(c_n^t(t) - c_{n,i}^s(t)\right) \pm \dfrac{N_c I}{zF} \\ V_t \dfrac{dc_n^t(t)}{dt} = N_S Q\left(\dfrac{1}{N_S}\sum_{i=1}^{N_s} c_{n,i}^s(t) - c_n^t(t)\right) \end{cases} \tag{9}$$

where $C_{n,i}^s$ denotes the concentration of the *n*th vanadium ion in the *i*th stack and N_s denotes the number of the stack.

However, during the operation of a multi-stack VRB, the transmission pipe of electrolyte is often very long, which is prone to electrolyte transfer delay. In this condition, the vanadium ion concentration at the tank's outlet might be very different from the vanadium concentration at the inlet of the stack. Therefore, the impact of the electrolyte transfer delay on the vanadium ion concentration cannot be ignored.

2.1.3 Electrolyte Transfer Delay

Electrolyte transfer delay is associated with fluid movement in the pipe. As the electrolyte is transferred through the pipe, there is a transfer delay in the delivery of the electrolyte.

For a single stack, the transfer time of the electrolyte from the tank outlet to the single stack is related to the pipe's length and flow rate, i.e.,

$$t_d = \frac{L_p}{v} = \frac{L_p \pi r_p^2}{Q} \tag{10}$$

where t_d denotes the transfer time from tank to stack; L_p denotes the pipe length; and r_P denotes the pipe radius.

For a multi-stack VRB module, the transfer time of the electrolyte from the tank outlet to the stack is the sum of the pipe sections the electrolyte flows through, i.e.,

$$t_d^i = \sum_{j=1}^{m^i} \frac{L_{ij}}{v_{ij}} = \sum_{j=1}^{m^i} \frac{L_{ij} \pi r_{ij}^2}{Q_{ij}} \tag{11}$$

where t_d^i denotes the transfer delay from the tank to the *i*th stack; m^i denotes the number of pipes from the tank to the *i*th stack; L_{ij} , r_{ij} , and Q_{ij} denote the pipe length, radius, and flow rate of the *j*th pipe between the tank and the ith stack, respectively.

Based on (9) and (11), the final vanadium ion concentration model for the multi-stack VRB considering the electrolyte transfer delay can be expressed as:

$$\begin{cases} V_s \dfrac{dc_{n,i}^s(t)}{dt} = Q\left(c_n^t(t - \sum_{j=1}^{m^i} \dfrac{\pi r_{i,j}^2 L_{i,j}}{Q_{i,j}}) - c_{n,i}^s(t) \right) \pm \dfrac{N_c I}{zF} \\ V_t \dfrac{dc_n^t(t)}{dt} = N_S Q\left(\dfrac{1}{N_S} \sum_{i=1}^{N_s} c_{n,i}^s \left(t - \sum_{j=1}^{m^i} \dfrac{\pi_{i,j}^2 L_{i,j}}{Q_{i,j}} \right) - c_n^t(t) \right) \end{cases} \tag{12}$$

where if $t < t_d^i$. We have,

$$c_n^t(t - \sum_{j=1}^{m^i} \frac{\pi r_{i,j}^2 L_{i,j}}{Q_{i,j}}) = c_n^t(0)$$

$$c_{n,i}^s \left(t - \sum_{j=1}^{m^i} \frac{\pi_{i,j}^2 L_{i,j}}{Q_{i,j}} \right) = c_{n,i}^s(0)$$

2.2 Results and Discussion

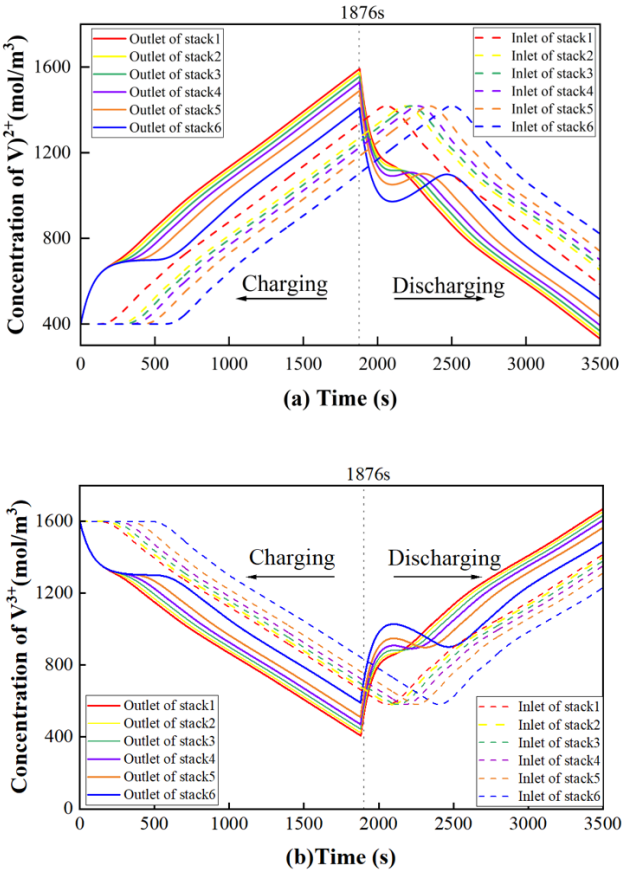

Fig. 5. Vanadium ion concentration in the multi-stack module. (a) Concentration of V2+. (b) Concentration of V3+.

To investigate the effect of electrolyte transfer delays on a multi-stack VRB module, a simulation model of a multi-stack VRB system consisting of six single-stack batteries connected in series was simulated, where every single stack consists of 60 cells. The module geometry and specifications are presented in Table Ⅱ.

In the simulation, charging and discharging experiments were carried out at a current density fixed at 100 mA/cm^2. The single cell was set to charge and discharge with a soc of between 20 and 80. Both the positive and negative electrolyte circulation pipes

Table II: Model Parameters

Parameters	Value
Electrode area, S	0.45 m²
Vanadium concentration, C_V	2 mol/L
Cell formal potential, E_0	1.4 V
The volume of electrolyte, V	4 m³
Flow rate, Q_0	5.6 L/s
Area resistance of a cell, R_Ω	0.0002 Ω·m²
Number of stacks in the module	6

are set up with a pipe length of 5 m between the tank and the first stack connected and a common pipe length of 2 m between each stack with a pipe radius of 0.15 m.

2.2.1 Concentration Distribution

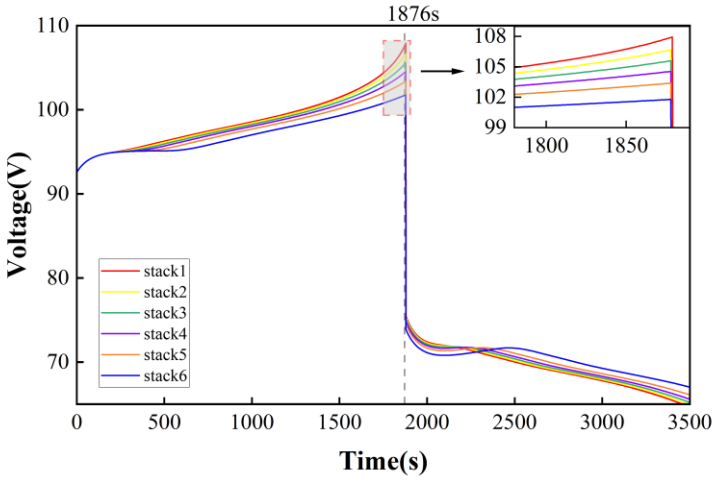

Fig. 6. Variation of stack voltages.

For a multi-stack VRB, the effect of electrolyte transfer delay on the distribution of electrolyte concentration is significant. Fig. 5 shows the variation of ion concentrations at different locations in the six stacks during one charge/discharge cycle. It can be observed that the trend of vanadium ion concentration with time is the same for all six stacks, but each stack has a certain time delay. This is because the six stacks are filled with the same electrolyte at the initial state. After the experiment, the electrolyte in the stack immediately undergoes electrochemical reactions and the concentration of V^{2+} rises and the concentration of V^{3+} decreases. The electrolyte flows into the storage tank through the pipe from the chimney outlet. However, due to the electrolyte transfer delay, both the vanadium ion concentrations at the inlet and outlet of each stack are inconsistent. Therefore, the concentration of vanadium ions in each stack maintains a certain level of difference.

As the reactant concentration in the stack directly affects the open circuit voltage and concentration overpotential of the battery, the difference in the ion concentration variation of each stack brought about by the electrolyte transfer delay directly leads to inconsistency in the voltage of each stack. When multi-stacks are connected in series, as shown in Fig. 6, and during the charging process, Stack 1, i.e., the one nearest to the tank, is the first to be fully charged, and other stacks will not be charged under the protection mechanism. Finally, the voltage difference between the maximum and minimum stack voltages is approximately 6 V. The discharge process is similar, which may lead to premature voltage cut-off during operation, resulting in poor capacity utilization of the battery as a whole.

2.2.2 Electrolyte Transfer Delay Influence Factor

Mathematically, the flow rate is critical to the electrolyte transfer delay and is also an important part of the operational control of the VRB battery. In Fig. 7(a), we used six flow rates to simulate the multi-stack VRB model, with the six flow rates being 1, 2, 3, 4, 5, and 10 times the flow rate Q_0 from Table II. As shown in Fig. 7(a), a higher flow rate leads to an improved battery consistency.

In addition to controlling the flow rate, we can also design the system pipes to reduce the impact of electrolyte transport delay. In this work, two groups of simulation experiments with different pipe lengths and different pipe radii (the pipes between stacks) are set up. As shown in Fig. 7(b), by comparing and analyzing the voltage balance of six stacks, the following conclusions are drawn: the longer the pipe length, the larger the pipe radius, and the more unbalanced the voltage of the multi-stack system. In addition, compared with the pipe length, the size of the pipe radius has a more significant impact on the voltage inconsistency.

Increasing the electrolyte circulation flow rate and shortening the length and radius of the pipe can effectively alleviate the electrolyte transfer delay, thus making the voltage distribution more balanced.

2.3 Conclusion

This work focuses on the effect of electrolyte transfer delay on the voltage characteristics of a multi-stack vanadium redox flow battery (VRB). Firstly, based on the transfer delay and the mass conservation equation, we establish a relationship between the reactant concentration in the tank and each stack as a function of time.

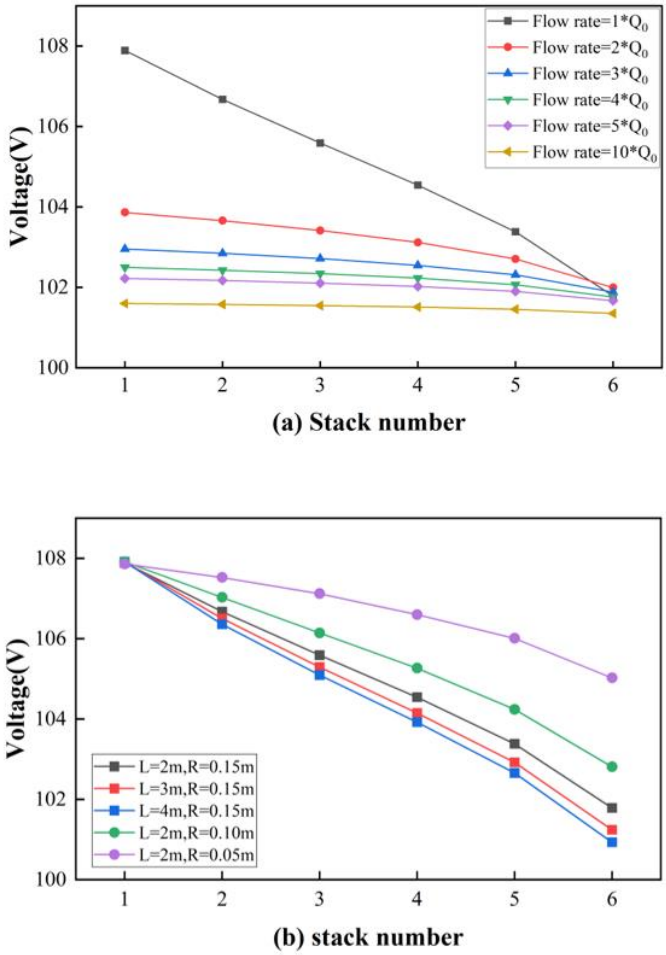

Fig. 7. Variation of stack voltages. (a) Under different flow rates. (b) Under different pipe design.

Next, based on the relationship, we analyze the effect of the electrolyte transfer delay on the ion concentration distribution. It is proven that the transfer delays and their negative impacts can be effectively reduced by optimizing the flow rates and the geometry of the pipes. Through the study of the effect of transmission delays on the voltage balance of multi-stack VRBs, design benchmarks and results can be used for future applications of large-scale VRB systems to improve the overall system efficiency of the batteries.

3. Peak Power Estimation Method of Vanadium Redox Flow Battery for Solar-Battery Powered Electric Vehicle Charging Stations

With the development and popularization of electric vehicles (EVs), the impacts of large-scale EV charging on the power system have emerged [21]. The photovoltaic (PV) and energy storage enhanced charging system is able to address the problem. The PV and energy storage charging system can mitigate the impact of high-power charging load on the grid system. Furthermore, it can actively contribute to establishing a dynamic balance between the ever-increasing urban electricity consumption load and distributed generation [22]. The schematic diagram of the PV and energy storage charging system based on VRB is shown in Fig. 8.

The VRB energy storage system stores electrical energy when the charging demand

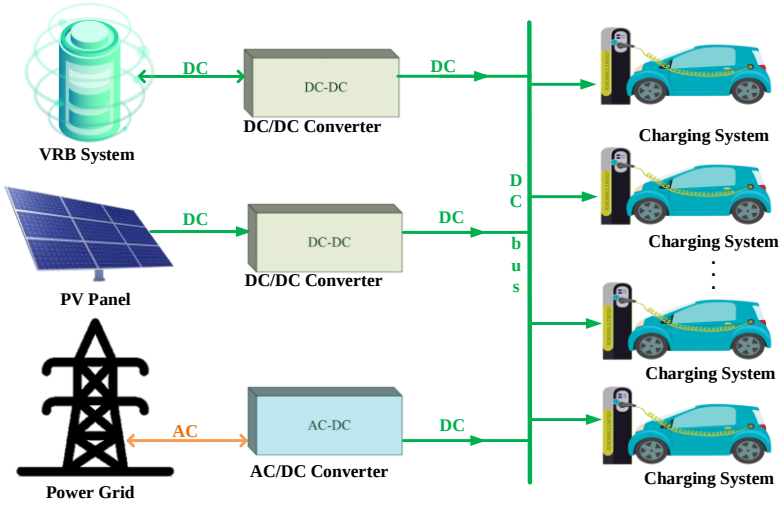

Fig. 8. Schematic of solar-battery powered electric vehicle charging.

is low and delivers the energy to the charging station when the charging demand is high, thereby realizing peak shifting [23-24]. The peak power is a parameter that characterizes the maximum ability of the battery to release or absorb power in a short period of time, which can provide a reference for power scheduling of the energy storage system [25]. Yu et al. [26] proposed a steady-state peak power estimation method based on a physical model of VRBs. However, this method only applies to the estimation of steady-state peak power in the design of a VRB stack, while it cannot be used to estimate peak power in the actual operation of VRBs. Wei et al. [27] considered the constraints of SOC, current, and terminal voltage on the peak power of VRB, proposed an estimation method, and verified the reliability and accuracy of the method based on complex working conditions. It should be noted that the analysis in the above literature ignores the influence of electrolyte flow rate on the peak power. Electrolyte flow rate, as a unique parameter of VRB, which is not available in other types of batteries, directly affects the stack power and pump power of VRB, thus indirectly affecting the output power of the VRB system. Adjusting the electrolyte flow rate is one of the ways to improve the power capability of VRB. Therefore, studying the influence of electrolyte flow on peak power can provide a reference for flow rate regulation and

make full use of the potential of VRB while ensuring the safe operation of VRB. In this work, an integrated equivalent circuit model is first developed. Then, a peak power estimation method is proposed. The VRB peak power is then evaluated under various flow rates and SOC.

3.1 Modeling of VRBs

The operating state of VRB is affected by many factors, such as the VRB system's temperature, current, and flow rates. Therefore, an accurate equivalent circuit model is necessary [28].

Among various existing VRB modeling methods, the integrated equivalent model of VRBs has shown high accuracy. This model consists of two parts, i.e., the equivalent electrical sub-model and the equivalent hydraulic sub-model. The equivalent electrical sub-model is used to describe the relationship between current, SOC, and voltage; and the equivalent hydraulic sub-model describes the relationship between the flow rate and the pump power. The two sub-models are coupled to each other through the flow rate of electrolytes, as illustrated in Fig. 9.

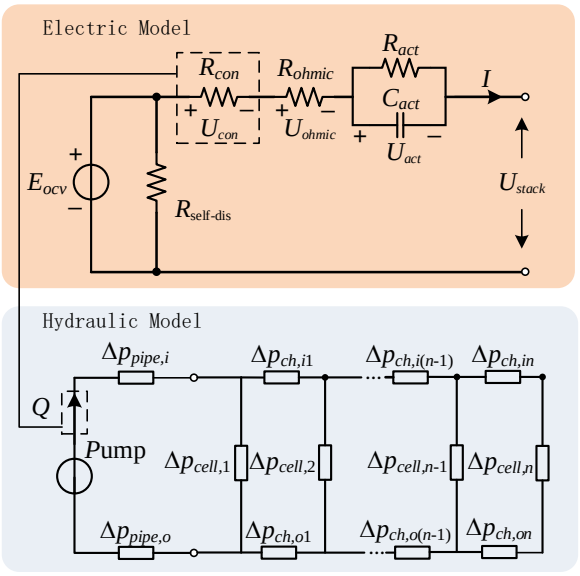

Fig. 9. Integrated equivalent circuit model of VRBs.

3.1.1 Electrical Sub-model

The electrical sub-model consists of five components:

1) A voltage source E_{ocv}, representing the OCV or the thermodynamic equilibrium. It is affected by the concentrations of various vanadium species and protons.
2) A resistance $R_{self\text{-}dis}$, used to describe the self-discharge phenomenon of VRB. It mainly refers to the leakage current generated by the active materials of the VRB positive and negative electrodes through the ion exchange membrane or through the internal and external public pipes.
3) A series-connected voltage U_{con}, which is caused by the difference in concentration

between the reactants on the electrode surface and the electrolyte reactants.

4) A series-connected voltage U_{ohmic}, which is the voltage drop generated by the current through the ohmic resistance. The ohmic resistance is generated from the contact resistance of the electrodes, electrolyte, diaphragm, and other components inside the stack.
5) A series-connected voltage U_{act}, which is caused by electrochemical polarization due to electron transfer. R_{act} and C_{act} represent the polarization resistance and polarization capacitance, respectively.

3.1.2 Hydraulic Sub-model

The electrolyte needs to be continuously pumped into the stack through the power pump [29]. The power provided by the pump is mainly used for the pressure loss in the liquid flow circuit. The relationship between the pump loss and electrolyte flow rate is calculated as follows:

$$P_{pump} = (\Delta p_{total} \times Q) / n_{pump} \tag{13}$$

where n_{pump} denotes the pump efficiency; and Δp_{total} denotes the total pressure drop in the VRB, which can be divided into two parts:

$$\Delta p_{total} = \Delta p_{pipe} + \Delta p_{stack} \tag{14}$$

where Δp_{pipe} denotes the pressure drop when the electrolytes run through the pipes; and Δp_{stack} denotes the pressure drop in the stack.

Based on the above integrated equivalent circuit model, the calculation formula of the model terminal voltage is as follows:

$$\text{Charge}: U_{stack} = E_{ocv} + U_{ohmic} + U_{act} + U_{con} \tag{15}$$

$$\text{Discharge}: U_{stack} = E_{ocv} - U_{ohmic} - U_{act} - U_{con} \tag{16}$$

3.2 EMPC-Based Peak Power Estimation

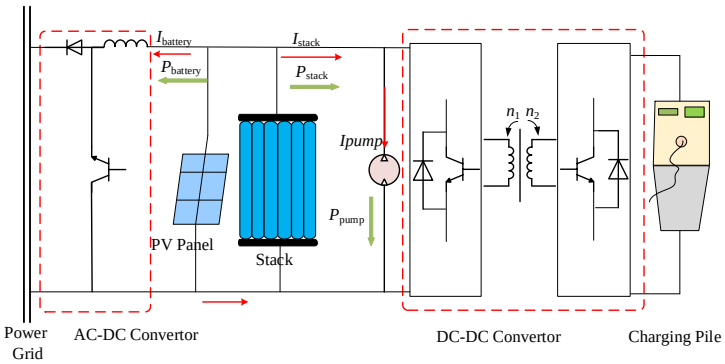

Fig.10. Energy conversion processes in a VRB system.

3.2.1 Definition of Peak Power

The VRB system is mainly composed of a stack, a pump, and a pipe, in which the

stack is the main part of the battery to provide power. As a unique feature of the VRB, the pump needs to absorb power to maintain the rotation of its internal motor and introduce the electrolyte into the stack. Therefore, the output power or absorbed power of VRB includes the stack power and pump power. In the actual operation of PV and energy storage systems based on VRB, the power flow diagram is shown in Fig. 10 [30].

The definition of the peak power of VRB is,

$$\text{Peak power} = \begin{cases} \max(P_{\text{stack}} - P_{\text{pump}}) & \text{Discharge} \\ \min(P_{\text{stack}} + P_{\text{pump}}) & \text{Charge} \end{cases} \tag{17}$$

where P_{stack} denotes the stack power; and P_{pump} denotes the pump power. P_{stack} is positive during discharge and negative during charge while P_{pump} as parasitic power loss is positive.

3.2.2 Predictive Model

According to the integrated equivalent circuit model, the state equation can be expressed as,

$$\begin{cases} SOC(t) = SOC_0 + \int_0^t \dfrac{\eta I(\tau)}{C_n} d\tau \\ C_{\text{act}} \dfrac{dU_{\text{act}}}{dt} + \dfrac{U_{\text{act}}}{R_{\text{act}}} = I \end{cases} \tag{18}$$

where t is the continuous-time index; I is the applied current; U_{stack} is the terminal voltage; and C_{n} is the nominal capacity of the VRB. In (16), the OCV is a function $f_{\text{ocv}}(\cdot)$ of SOC ,i.e.,

$$E_{\text{ocv}} = E_0 + \frac{RT_{\text{stack}}}{zF}\left[k_1 \text{In}(\text{SOC}) - k_2 \text{In}(1-\text{SOC})\right] \tag{19}$$

where E_0 is the formal potential; R represents the universal gas constant; F is Faraday's constant; and z is the number of electrons transferred. k_1 and k_2 are two correction coefficients. T_{stack} is the electrolyte temperature in the stack. The relationship between OCV and SOC can be calculated by first-order Taylor series polynomial:

$$E_{\text{ocv},k+1} \approx E_{\text{ocv},k} + f'_{\text{ocv}}(\text{SOC}_k)(\text{SOC}_{k+1} - \text{SOC}_k) \tag{20}$$

where f'_{ocv} represents the derivative function of $f_{\text{ocv}}(\cdot)$. According to (18), the SOC's discrete form expressions can be expressed as

$$\text{SOC}_{k+1} = \text{SOC}_k - \eta I_k \Delta t / C_n \tag{21}$$

Substituting (21) into (20), we have

$$E_{\text{ocv},k+1} = -(\eta \Delta t / C_n) f'(\text{SOC}_k) I_k + E_{\text{ocv},k} \tag{22}$$

To sum up, the model state equation and output equation are summarized as follows:

$$\chi_{k+1} = \underbrace{\begin{bmatrix} 1 & 0 & 0 \\ 0 & e^{-\Delta t/R_1C_1} & 0 \\ 0 & 0 & 1 \end{bmatrix}}_{A} \chi_k + \underbrace{\begin{bmatrix} -\Delta t / C_n \\ 1 - e^{-\Delta t/R_1C_1} \\ -f'_{\text{ocv}}(\text{SOC}_k)\eta \Delta t / C_n \end{bmatrix}}_{B} u_k \tag{23}$$

$$y_k = \underbrace{\begin{bmatrix} 0 & -1 & 1 \end{bmatrix}}_{\tilde{C}} \chi_k + \underbrace{(-R_0)}_{\tilde{D}} u_k - U_{\text{con},k} \tag{24}$$

where $\chi = [\text{SOC}, U_{act}, E_{\text{ocv}}]^T$ is the state vector; $y_k = U_{t,k}$ is the voltage output; and $u_k = I_k$ is the current input. U_{con} is a nonlinear function of current and flow rate, so it cannot be merged with the matrix $\tilde{D}$. Equations (23) and (24) will be used next as the predictive model in the proposed EMPC peak power estimator [33].

3.2.3 Constrained Optimization Problem

The task for peak power estimation is to calculate the maximum accumulated power over a future time horizon *N* [34].

$$J = \max_{\vec{u}^N} \left(\sum_{i=1}^{N} \left(u_{k+i} y_{k+i} - P(Q) \right) \right) \tag{25}$$

where *J* represents the cost of the objective function; *y* is the terminal voltage; u is the input current; and *P* is the pump loss, which is a function of the flow rate. Therefore, the objective function is established to transform the estimation of peak power into an optimization problem of current and flow rate, where the current and flow rate are the optimization variables, and the control objective is to look for a set of input current and flow rate sequences to achieve the maximum charging and discharging power.

In addition, VRB peak power is limited by many factors. First, the battery current is limited by the ratings of cables, fuses, power converters, etc. Here, we assume the current should be limited between I_{min} and I_{max}. Next, The flow rate is limited by the speed of the pump. We assume the flow rate should be limited in between Q_{min} and $Q_{\text{max.}}$ Next, the VRB should also avoid over-charge and over-discharge, so it needs to operate within a safe range of SOC and voltage limited by [SOC_{min}, SOC_{max}] and [$U_{\text{t,min}}$, $U_{\text{t,max}}$]. In summary, the constraints of the objective function are summarized as follows:

$$\begin{cases} I_{\text{min}} \le u_{k+i} \le I_{\text{max}} \\ Q_{\text{min}} \le Q_{k+i} \le Q_{\text{max}} \\ U_{t,\text{min}} \le y_{k+i} \le U_{t,\text{max}} \\ \text{SOC}_{\text{min}} \le s_{k+i} \le \text{SOC}_{\text{max}} \end{cases} \tag{26}$$

where s represents the SOC for brevity.

According to the above model state equation, the state matrix can be written as follows [31-32]:

$$\vec{\chi}^N = p\chi_k + q\vec{u}^N \tag{27}$$

where

$$\vec{\chi}^N = \begin{bmatrix} \chi_{k+1} \\ \chi_{k+2} \\ \vdots \\ \chi_{k+N} \end{bmatrix}, \quad p = \begin{bmatrix} \tilde{A} \\ \tilde{A}^2 \\ \vdots \\ \tilde{A}^N \end{bmatrix}, \quad q = \begin{bmatrix} \tilde{B} & 0 & \cdots & 0 \\ \tilde{A}\tilde{B} & \tilde{B} & \cdots & 0 \\ \vdots & \vdots & \ddots & 0 \\ \tilde{A}^{N-1}B & \tilde{A}^{N-2}\tilde{B} & \cdots & \tilde{B} \end{bmatrix}$$

The predicted terminal voltage vector can be obtained as,

$$\vec{y}^N = f\chi_k + g\vec{u}^N - h \tag{28}$$

where

$$\vec{y}^N = \begin{bmatrix} y_{k+1} \\ y_{k+2} \\ y_{k+3} \\ \vdots \\ y_{k+M} \end{bmatrix},\ f = \begin{bmatrix} \tilde{C}\tilde{A} \\ \tilde{C}\tilde{A}^2 \\ \tilde{C}\tilde{A}^3 \\ \vdots \\ \tilde{C}\tilde{A}^M \end{bmatrix},\ h = \begin{bmatrix} P(Q_{k+1}) \\ P(Q_{k+2}) \\ P(Q_{k+3}) \\ \vdots \\ P(Q_{k+M}) \end{bmatrix},\ g = \begin{bmatrix} \tilde{C}\tilde{B} & \tilde{D} & 0 & \cdots & 0 \\ \tilde{C}\tilde{A}B & \tilde{C}\tilde{B} & \tilde{D} & \cdots & 0 \\ \tilde{C}\tilde{A}^2\tilde{B} & \tilde{C}\tilde{A}\tilde{B} & \tilde{C}\tilde{B} & \cdots & 0 \\ \vdots & \vdots & \vdots & \ddots & \vdots \\ \tilde{C}\tilde{A}^{N-1}\tilde{B} & \tilde{C}\tilde{A}^{N-2}\tilde{B} & \tilde{C}\tilde{A}^{N-3}\tilde{B} & \cdots & \tilde{D} \end{bmatrix}$$

Substitute the predicted model terminal voltage into the objective function, and simplify *J* as follows:

$$\max_{\vec{u}^N} J = \max_{\vec{u}^N}\left(\sum_{i=1}^{N}\left(u_{k+i}y_{k+i}\right) - P(Q)\right) \Rightarrow \min_{\vec{u}^N}\left(-\left|\vec{u}^N\vec{y}^N - \vec{P}_Q^N\right|\right) \tag{29}$$

where $\vec{P}_Q^N$ is the pump loss vector in N dimensions.

In addition, while optimizing the objective function, the constraint conditions should be transformed into the functions of input variables. Since the current and the flow rate are input variables in the constraint conditions, they do not need to be transformed. Only the terminal voltage and SOC need to be transformed as they are functions of input variables. The specific steps are given as follows:

First, simplify the terminal voltage constraints. Consider the constraint range of the battery terminal voltage:

$$\begin{bmatrix} f\chi_k + g\vec{u}^N - h \\ -(f\chi_k + g\vec{u}^N - h) \end{bmatrix} \le \begin{bmatrix} \vec{y}_{\max}^N \\ -\vec{y}_{\min}^N \end{bmatrix} \tag{30}$$

where $\vec{y}_{\max}^N \in \mathbb{R}^N$ and $\vec{y}_{\min}^N \in \mathbb{R}^N$ contain the upper voltage limit $U_{t,max}$ and the lower voltage limit $U_{t,min}$ mentioned in (26).

Next, the SOC sequence $\vec{z}^N$ can be expressed as,

$$\vec{z}^N = H(p\chi_k + q\vec{u}^N) \tag{31}$$

where $H = \mathrm{diag}(\underbrace{[E_1,\ E_1,\ \cdots\ E_1]}_{N})$ and $E_1 = [1\ \ 0\ \ 0]$.

By substituting (31) into (26), the constraint on SOC could be expressed as,

$$\begin{bmatrix} Hq \\ -Hq \end{bmatrix}\vec{u}^N \le \begin{bmatrix} \vec{z}_{\max}^N - Hpx_k \\ -(\vec{z}_{\min}^N - Hpx_k) \end{bmatrix} \tag{32}$$

where $\vec{z}_{\max}^N \in \mathbb{R}^N$ contains the upper SOC limit SOC_{max} and $\vec{z}_{\min}^N \in \mathbb{R}^N$ contains the lower SOC limit SOC_{min}.

Next, the constraint for current and flow rate could be expressed as follows,

$$\begin{bmatrix} \vec{u}^N \\ \vec{u}^N \\ \vec{Q}^N \\ \vec{Q}^N \end{bmatrix} \leq \begin{bmatrix} \vec{I}_{\max}^N \\ -\vec{I}_{\min}^N \\ \vec{Q}_{\max}^N \\ -\vec{Q}_{\min}^N \end{bmatrix} \tag{33}$$

where $\vec{I}_{\max}^N \in \square^N$, $\vec{Q}_{\max}^N \in \square^N$ and $\vec{I}_{\min}^N \in \square^N$ are the upper and lower limits of the current and flow rate.

To realize the optimization of current and flow rate, we use the function f_{mincon} based on a sequential quadratic programming algorithm in MATLAB to solve the VRB terminal voltage sequence $\vec{y}^{N*} = [U_{t,k+1}^*, \cdots U_{t,k+N}^*]$ which can be estimated by (28). When the current sequence $\vec{u}^{N*}$ is obtained, multiplying $\vec{u}^{N*}$ by $\vec{y}^{N*}$ yields the peak power sequence, denoted by $\left[P_{k+1}^{\text{dis}*}, P_{k+2}^{\text{dis}*}, ..., P_{k+M}^{\text{dis}*}\right]$ for discharging and $\left[P_{k+1}^{\text{chg}*}, P_{k+2}^{\text{chg}*}, ..., P_{k+M}^{\text{chg}*}\right]$ for charging, respectively. The instantaneous peak power at time instant k is expressed as follows:

$$\begin{cases} P_{\text{peak},k}^{\text{dis}} = \min(P_{k+1}^{\text{dis}*}, P_{k+2}^{\text{dis}*}, ..., P_{k+M}^{\text{dis}*}) \\ P_{\text{peak},k}^{\text{chg}} = \max(P_{k+1}^{\text{chg}*}, P_{k+2}^{\text{chg}*}, ..., P_{k+M}^{\text{chg}*}) \end{cases} \tag{34}$$

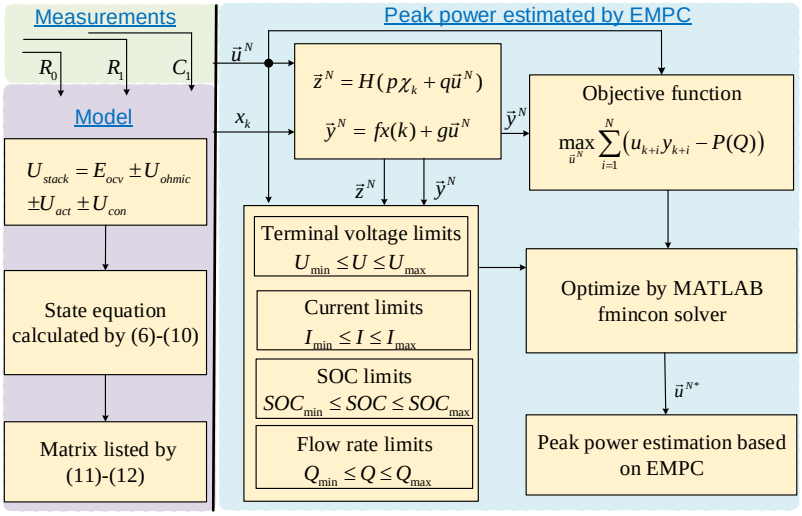

Fig.11. Framework of proposed peak power estimation scheme for VRBs.

The steps of peak power estimation are shown in Fig. 11.

Step 1: Measure the value of R_0, R_1, and C_1.

Step 2: Calculate the state and terminal voltage over the prediction horizon N according to (23) and (24).

Step 3: Establish the objective function in the form of (17) and the constraint inequality in the form of (30)-(33).

Step 4: Use the f_{mincon} solver to optimize the current and flow rate and substitute them into (28) to calculate the terminal voltage. Finally, estimate the peak power of each period according to (34).

The above steps are the estimation process in a cycle. Repeating them can realize the estimation of peak power.

3.3 Simulation Results

In this section, we use the peak power estimator based on EMPC to estimate the corresponding peak power. The specifications of the simulation parameters are shown in Table III.

The results under the constant flow rate and different SOC are shown in Fig. 12.

Table III: Specifications of the Simulation Parameters

Parameter	Symbol	Value
Correction coefficient	k_1	1.1
	k_2	1.0
Faraday constant	F	96,485 C·mol^{-1}
Gas constant	R	8.31J·mol^{-1}·K^{-1}
Temperature	T	303 K
Ohmic resistance	R_0	0.048 Ω
Activation resistance	R_1	0.0089 Ω
Activate capacitance	C_1	1000 F
Terminal voltage limits	U_{min}	40 V
	U_{max}	60 V
Current limits	I_{min}	-100 A
	I_{max}	100 A
State of charge	SOC_{min}	0.1
	SOC_{max}	0.9
Flow rate limits	Q_{min}	100 cm^3·s^{-1}
	Q_{max}	100 cm^3·s^{-1}

The discharging peak power increases gradually as the corresponding terminal voltage

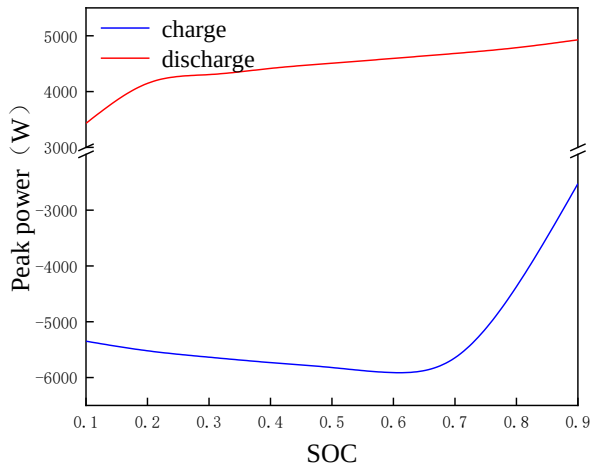

Fig.12. Simulation estimation results of peak power.

increases with the increase of SOC while the current is limited by the maximum current. The charging peak power first increases and then decreases with SOC. The underlying reason is that the remaining power of the battery is relatively low within the SOC range of 0.1 to 0.6. At this time, the charging peak power is constrained by the rated current of the battery, and the corresponding terminal voltage will increase with the increase of SOC under the same peak current. Therefore, the charging peak power increases gradually. The charging peak power of the battery is constrained by the range of terminal voltage and SOC = 0.6-0.9. During this time, the corresponding peak current will decrease with the increase of SOC so that the charging peak power will decrease. At the same time, we know that the flow rate also impacts the peak power, which cannot be ignored. Therefore, we have simulated under different flow rates, and the

results are shown in Fig. 13.

As can be seen from the figure that in the discharging mode, the peak power increases with an increasing flow rate at SOC=0.1. This increases first at SOC = 0.2 and reaches

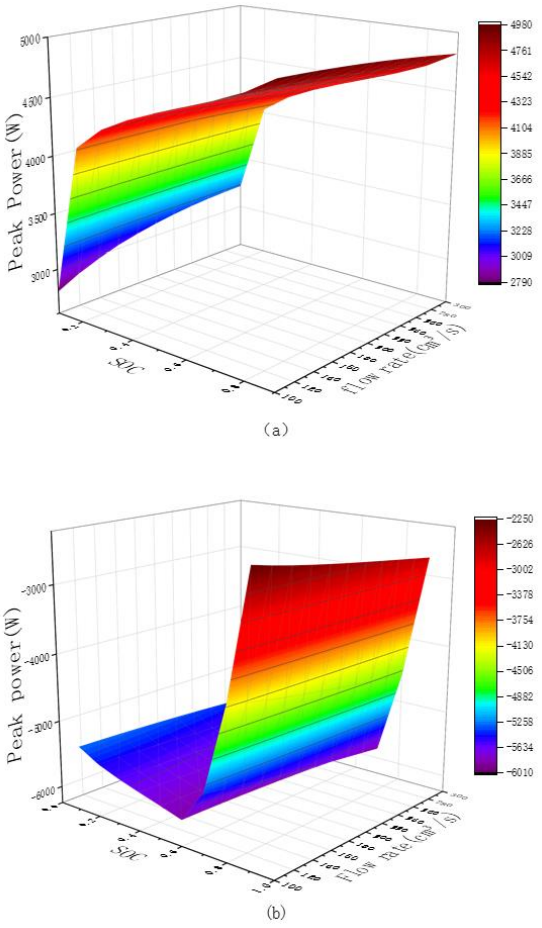

Fig.13. Simulation estimation results of peak power under variable flow rate. (a) Under discharging mode. (b) Under charging mode.

its peak at a flow rate=140 cm³/s then decreases with increasing flow rate after SOC = 0.3. While in the charging mode, the peak power increases with the increase of the flow rate. This is because the pump losses are a quadratic function of the flow rate [35]. The higher the flow rate, the higher the pump loss. According to (29), in the discharging state at low SOC, the increase in flow rate causes a significant increase in the value of the stack voltage. The current remains constant because it is limited, and the pump losses increase slightly slower than the increase of stack voltage, so the peak power increases first and then decreases. At high SOC, the stack voltage remains constant, and the pump loss continues to increase with the increase in flow rate, so the peak power decreases. In the charging mode, the flow rate increases so that the charging current increases slightly, and the voltage remains the same as the open circuit voltage. The pump loss increases significantly, so the peak power increases. Based on the simulated peak power area shown in Fig. 13, we can obtain the maximum capacity of the VRB energy storage system that can absorb/release power, thus ensuring the VRB system can operate in a safe and stable condition.

3.4 Conclusion

This paper presents a new method based on EMPC to achieve a high-accuracy estimation of VRB peak power. Compared with the traditional method, this method considers the effect of the pump on the system and thus considers the influence of different flow rates on the performance of VRB. The simulation results show that the discharging peak power increases with the increase of SOC to a peak and then decreases with the increase of flow rate. The charging peak power first increases and then decreases with the increase of SOC and increases with the increase of flow rate. It ensures the normal operation of the energy storage system when many electric vehicles are charged at the same time.

4. Microgrid Control Method Based on Virtual Synchronous Machines in Islanded Mode

As the goal for decarbonization and expansion of renewable energies, traditional power systems find it challenging to meet customers' diverse power demands and high-reliability requirements. Renewable energy-based distributed generation is gradually becoming a research focus [35]. Distributed renewable energy generation can reduce environmental pollution, promote the diversification of primary energy sources, improve the overall efficiency of energy use and enhance the security and reliability of power supply compared to traditional power generation models [37]. Microgrids are proposed to take full advantage of distributed generation, which can fully integrate the advantages of resources and reduce the impact of secondary energy access on grid stability. It can operate in either grid-connected mode or islanded mode, with grid-connected mode operation providing bi-directional power exchange with the grid and islanded mode providing high quality, uninterrupted power to the load [38].

Distributed power sources are commonly connected to microgrids via inverters. Although inverters have the advantage of rapid response, the proportion of synchronous generators continues to decrease as distributed power sources are connected on a large scale, leading to increasingly severe stability challenges for the grid [39]. The Virtual Synchronous Machine (VSM) allows the inverter to have similar moments of inertia and damping characteristics to the synchronous generator. With the VSM, The inverter can simulate the external characteristics of the synchronous generator's output. This helps to ensure the stable operation of the microgrid and reduce the unstable impact brought by distributed energy resources [40].

Many research works investigated the application of VSM in microgrids and analyzed the key VSM technologies such as off-grid, parallel, and parallel-off-grid switching of individual VSMs, but did not mention VSM in parallel connection. In [41], an off-grid operation strategy was proposed for microgrids consisting of multiple VSMs in parallel and introduced the power distribution in island mode. In [42], an adaptive rotational inertia control methodology was proposed to improve the stability of multiple VSMs in parallel operation by changing the magnitude of rotational inertia according to the load changes. In [43], the effect of rotational inertia on the inverter's individual output quantities such as frequency and active power was investigated when multiple VSMs were operated in parallel. The adjustment of the rotational inertia was also proposed to improve the stability of the multi-VSM operating condition under different operating conditions. In [44], a differential-free frequency regulation control strategy based on VSM control was proposed. This enables secondary frequency modulation of the system and accurate power distribution. A virtual inertia matching method for the multiple VSMs was proposed in [45]. However, the relationships between key parameters such as rotational inertia and damping coefficient applicable to the parallel operation of VSMs of different capacities are not given.

However, the above papers do not discuss the issue of parallel connection of different capacity VSMs, especially the frequency response and power sharing during system load changes are not considered. The fact that it is an issue that needs to be considered when multiple VSMs are operating in parallel, where dynamic performance may vary, and power allocation errors may occur during system load changes [46]–[48].

In this work, the control strategy of VSMs with different rated capacities in parallel operation is studied. Firstly, a microgrid VSM control strategy is introduced. This can reduce the voltage transients under the island operation mode and achieve a smooth transition when the load changes compared with the traditional control method. A single VSM simulation model is established to validate the effectiveness of the proposed control strategy. Then a simulation model is built for parallel operation of three different capacities of VSM, and the effectiveness of the control strategy under the parallel operation of multiple VSMs is verified by the simulation.

4.1 Control Method of Virtual Synchronous Machine VSM Control Strategy

The implementation of VSM control is key to the need to simulate the damping and inertia characteristics of synchronous generators, so that the inverter has similar external characteristics to synchronous generators, thus improving the stability and safety of microgrid operation.

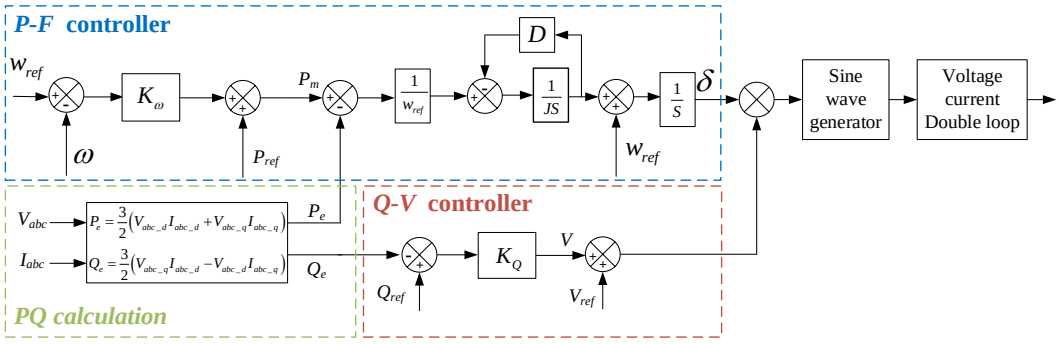

Fig. 14. Block diagram of the VSM control strategy.

A typical VSM control strategy is illustrated in Fig 14. The control strategy of the VSM consists of a PQ calculation module, a P-F controller, a Q-V controller, a sine wave generator, and a voltage and current control dual loop.

4.1.1 *P-Q* Calculation

The real-time active power P_e and real-time reactive power Q_e output by the inverter based on VSM can be calculated from the dc/ac converter's real-time output current I_{abc} and the real-time output voltage V_{abc}.

$$\begin{cases} P_e = 1.5\left(V_{abc\_d}I_{abc\_d} + V_{abc\_q}I_{abc\_q}\right) \\ Q_e = 1.5\left(V_{abc\_q}I_{abc\_d} - V_{abc\_d}I_{abc\_q}\right) \end{cases} \tag{35}$$

where V_{abc_d} and V_{abc_q} are the *d* and *q*-axis components of the *dq* coordinate system in

the conversion of V_{abc} into a *dq* coordinate system; and I_{abc_d} and I_{abc_q} are the d and q-axis components of I_{abc} in the conversion of Iabc into a dq coordinate system, respectively.

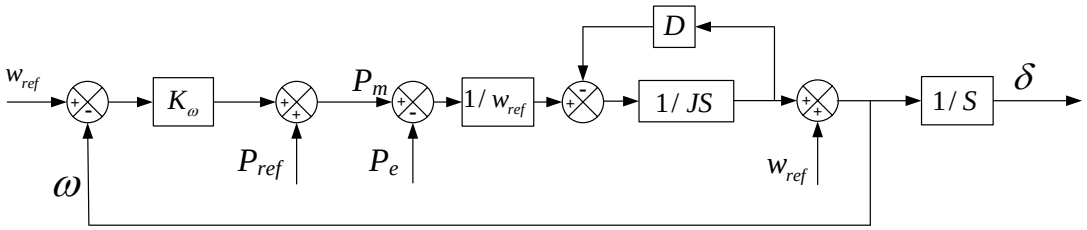

Fig. 15. P-F controller diagram of VSM.

4.1.2 *P-F* Controller

The VSM control module is composed of a *P-F* controller and a *Q-V* controller. The *P-F* controller diagram of VSM is illustrated in Fig. 15, and it mainly consists of a *P-F* adjustment part and a mechanical part. The primary function of the *P-F* regulation part is to adjust the virtual mechanical power, which can be described as follows:

$$P_m = P_{ref} + k_w(w_{ref} - w) \tag{36}$$

where P_m represents the mechanical power of VSM; P_{ref} denotes the nominal frequency; and k_w represents the active sag factor. The rotor motion equation is a key part of the *P-F* controller and an essential part of the simulation of synchronous generator rotor motion. The specific mathematical expressions are shown below.

$$\begin{cases} J\dfrac{d\Delta w}{dt} = \dfrac{P_m}{w_{ref}} - \dfrac{P_e}{w_{ref}} - D\Delta w \\ \Delta w = w - w_{ref} \end{cases} \tag{37}$$

where J and D denote the rotational inertia and the damping factor of the generator, respectively; w_{ref} and w denote the rated angular velocity and the actual angular velocity, respectively; and P_e indicates the instantaneous power of the inverter.

4.1.3 *Q-V* Controller

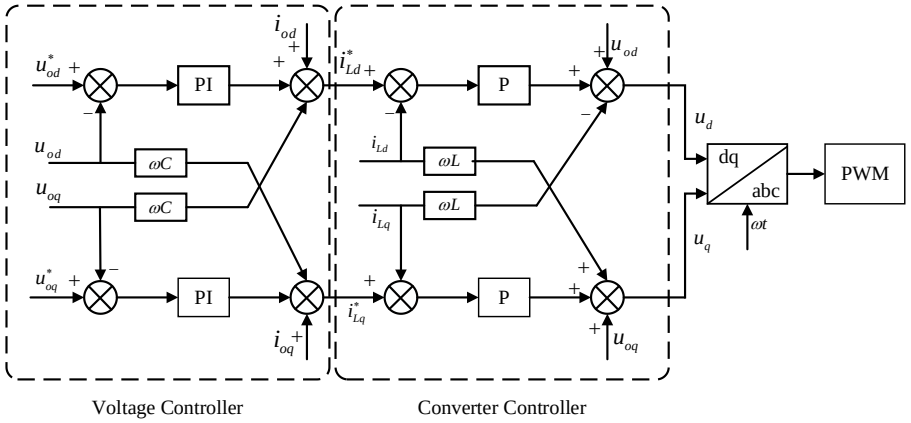

Fig.16. Dual-loop voltage and current control diagram.

The *Q-V* controller section in the VSM control system has a reactive-voltage regulation function, which mainly refers to the reactive-voltage sag curve of the synchronous

generator for voltage regulation:

$$V = V_{ref} + k_Q(Q_{ref} - Q_e) \tag{38}$$

where V_{ref} represents the rated voltage; Q_{ref} represents the rated reactive power; and k_Q denotes the reactive-voltage droop factor.

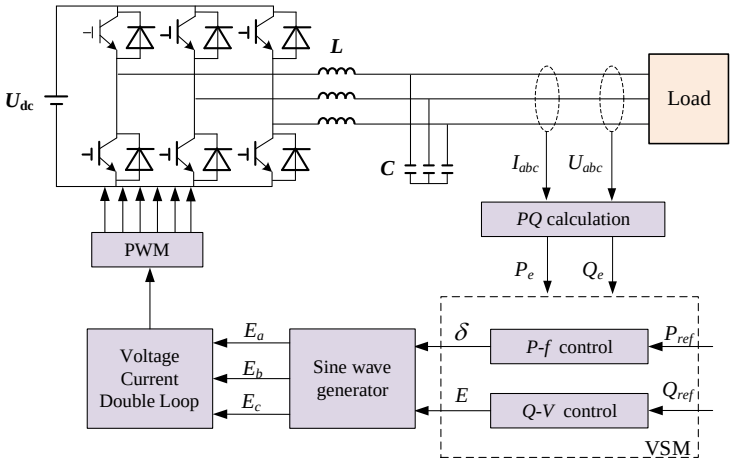

Fig.17. Single inverter based on VSM control strategy.

4.1.4 Sine Wave Generator

The phase angle at the output of the *P-F* controller and the voltage amplitude at the output of the *Q-V* controller are used as the phase and amplitude of the reference voltage, respectively. Then the voltage vector U_{abc} of the reference voltage at the output of the VSM can be obtained by modulating it with a three-phase sine wave.

$$U_{abc} = \begin{bmatrix} E_u \sin\delta \\ E_u \sin(\delta - 2\pi/3) \\ E_u \sin(\delta + 2\pi/3) \end{bmatrix} \tag{39}$$

4.1.5 Dual-Loop Voltage and Current Control Diagram

To reduce disturbing signals in the control signal, the control signal is regulated by two closed loops, the voltage closed loop as well as the current closed loop. It is then modulated by PWM in the circuit of the inverter. The dual-loop voltage and current control diagram is shown in Fig. 16.

4.2 Dynamic Characteristics of Inverter Based on VSM

In this section, the single-inverter and three-inverter parallel models based on VSM are built in the MATLAB/Simulink R2021a environment, respectively. This is to demonstrate the dynamic operating characteristics of single inverters based on VSM and the frequency response and power distribution of multiple inverters operating in parallel.

4.2.1 Simulation and Analysis of Single Inverter Operation Based on VSM

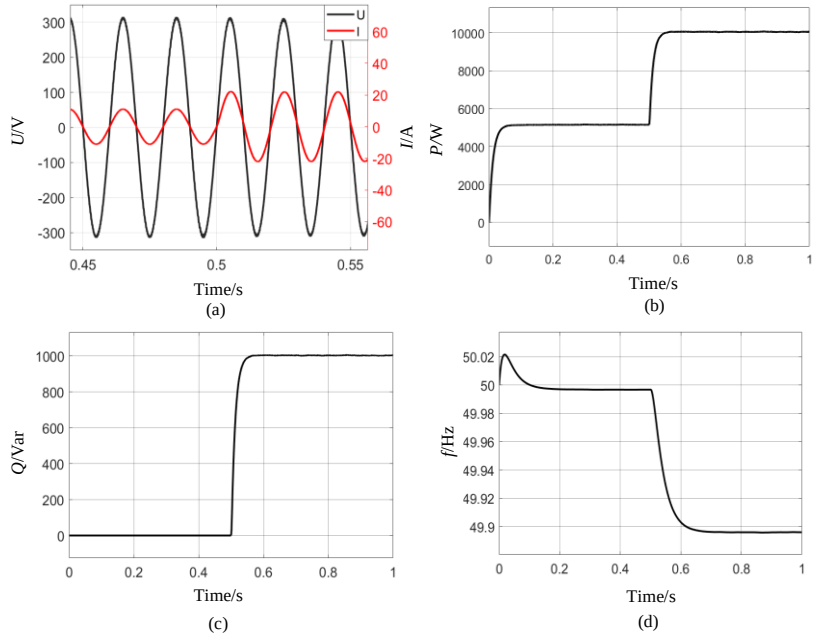

Fig.18. Change in system output as the load changes. (a) Changes in system voltage and current;(b) Changes in system active power output; (c) Changes in system reactive power output; (d) Changes in system frequency.

The single inverter based on VSM is shown in Fig. 17, and the whole system is composed of the main line and control section.

In this section, the single inverter based on the VSM is established and simulated using the main parameters of the single system shown in Table IV. The results of the simulation of the inverter based on the VSM operating independently when the load is increased from 5 kW/0 kVAr to 10 kW/1 kVAr at t = 0.5 s are shown in Fig. 18. Fig. 18(a) represents the changes in system voltage and current. Fig. 18(b) represents the changes in system active power output. Fig. 18(c) represents the changes in system reactive power output, and Fig. 18(d) represents the changes in system frequency. It is evident from Fig. 18(d) that when the load increases, the frequency variation range is stable within 0.2 Hz. Due to the VSM simulating the rotational inertia and damping characteristics of a synchronous generator, the frequency changes smoothly when the

Table IV: Main Parameters of the System

Parameter	Value
DC voltage	800 V
Rated voltage	380 V
Filter capacitance	15 μF
Rated frequency	50Hz
Filter inductance	3 mH
Rated reactive power	1 kVar
Rated active power	5 kW

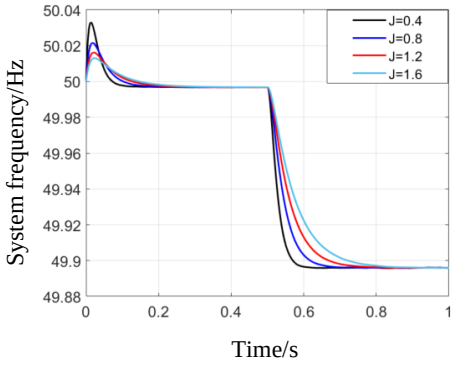

(a)

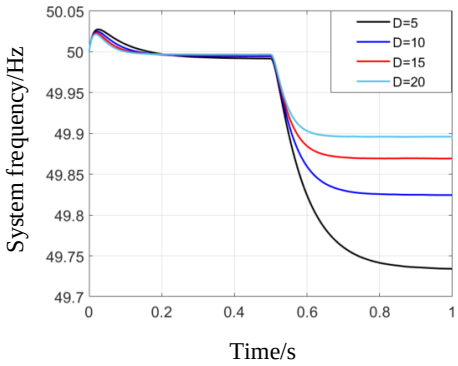

(b)

Fig.19. Frequency response of the system for different coefficients of inertia and damping. (a) System frequency responses under various moments of inertia. (b) System frequency responses under various damping coefficients.

system load changes. The active and reactive power output of the inverter varies with the load.

Fig. 19 represents the effect of rotational inertia J and damping factor *D* on frequency variation. Fig. 19(a) shows the effect of the magnitude of the rotational inertia on the output frequency. For the same load conditions and constant steady-state value, the larger the rotational inertia *J*, the longer the dynamic response time for the system to reach steady state again. Fig. 19(b) shows the effect of damping coefficient *D* on the

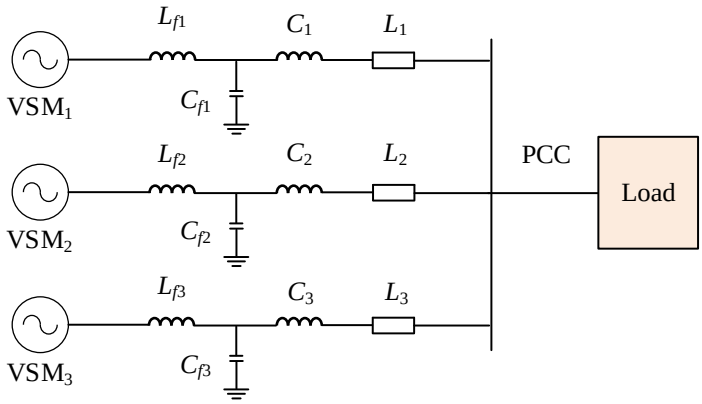

Fig.20. A schematic diagram of the parallel connection of three inverters based on VSM.

output frequency stability in the system. The final stable value of the frequency is different for different damping factors, and the above results are consistent with the characteristics of synchronous generators.

4.2.2 Simulation and Analysis of Three Inverters Operation Based on VSM

A schematic diagram of the parallel connection of three inverters based on VSM is illustrated in Fig. 20. The main parameters of the parallel system are included in the following Table V.

Table V: Main Parameters the Parallel System

Parameter	VSM_1	VSM_2	VSM_3
DC voltage/V	1000	1000	1000
Moment of inertia *J/Kg/m2*	5	3	2
Rated reactive power/kVar	50	30	20
Rated voltage/V	600	600	600
Rated frequency/Hz	60	60	60
Rated active power/kW	250	150	100
Damping coefficient *D/N.m.s/rad*	25	15	10

The application of the VSM control strategy in a multi-source parallel microgrid disconnected from the main grid means that autonomous operation is possible while disconnected from the main grid. The microgrid consists of three distributed power sub-systems in parallel, set at a rated power of 500 kW, 300 kW and 200 kW respectively.

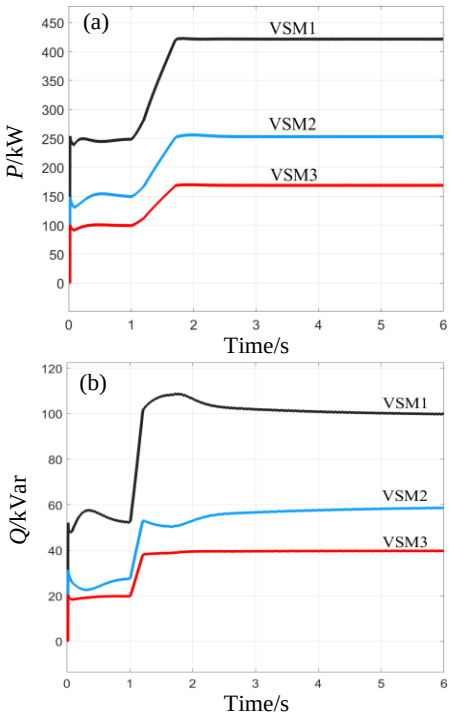

Fig.21. Change in output active and reactive power of the three VSM. (a) Active power output change; (b) Reactive power output change.

They are connected to a unified node and ultimately to the total load. The total microgrid load is controlled and regulated by a dynamic load model. Each sub-system is represented by a DC source as a typical distributed generation system, such as photovoltaic, wind power, etc. Each sub-system also includes a VSM-based control system and a PWM generator supplying power to the inverter.

The total system load gradually increases from 500 kW/100 kVAr to 850 kW/200 kVAr at 1 s. The variations of the output active and reactive power of the three VSMs are illustrated in Fig 21. As illustrated in Fig. 21(a), the output active power of VSM_1, VSM_2, and VSM_3 in the initial test state are 250 kW, 150 kW, and 100 kW, respectively. The total load is shared by the three inverters in proportion to their rated capacity when the load increases. The output active power values of VSM_1, VSM_2, and VSM_3 are 425 kW, 255 kW, and 170 kW, respectively. As shown in Fig 21(b), under the initial test conditions, the output reactive power values of VSM_1, VSM_2, and VSM3 are 50 kVAr, 30 kVAr, and 20 kVAr, respectively. The output power ratio of the three VSMs is maintained at 5:3:2. These results show that the three inverters can follow the load changes and share the power among them.

Fig. 22 shows the system frequency versus voltage variation curve. As shown in Fig. 22(a), the system was operating at the rated condition before t = 1 s with the frequency maintained at 60 Hz. After t = 1 s, the frequency decreases as the load increases until it is maintained at 59.8 Hz. As shown in Fig. 22(b), the system is rated at 600 V, and after t = 1 s, the voltage decreases as the load increases, eventually stabilizing at 595 V due to the VSM.

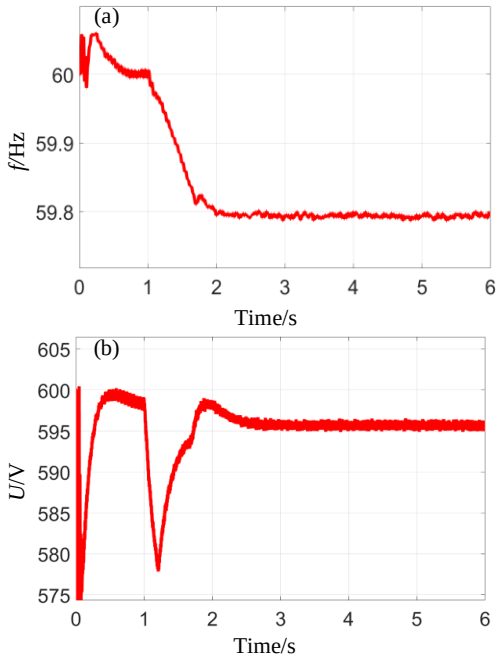

Fig.22. System output change during load change. (a) Frequency change of system; (b) Voltage change of system.

4.3 Conclusion

In this work, the VSM control is applied to the control strategy of parallel inverters and is simulated in MATLAB/Simulink for a single inverter and three inverters in islanded mode. The simulation results indicate that the inverters based on the VSM control strategy can track the changes of load and that the active and reactive power of the load can be shared precisely according to the ratio of the rated capacity of each inverter when multiple inverters are operated in parallel. As the VSM simulates the rotational inertia and damping characteristics of a synchronous generator, the system frequency can be changed smoothly when the load changes, thus improving the immunity and reliability of the system. As distributed power supplies become more popular, the VSM-based multi-inverter parallel control strategy will be widely implemented

References

[1] J. P. Xi, “Statement at the general debate of the 75th session of the United Nations general assembly,” Gazette of the State Council of the People’s Republic of China, vol. 28, pp., 5-7, 2020.

[2] Y. B. Shu, L. Y. Zhang, Y. Z. Zhang, et al., “Carbon peak and carbon neutrality path for China’s power industry,” Strateg. Study CAE, vol. 23, pp. 1-14, 2021.

[3] M. Li, Y. Li, and S. S. Choi, “Dispatch planning of wide-area wind power-energy storage scheme based on ensemble empirical mode decomposition technique,” IEEE Trans. Sustain. Energy, vol. 12, no. 2, pp. 1275-1288, Apr. 2021, doi: 10.1109/TSTE.2020.3042385.

[4] M. Skyllas-Kazacos, G. Kazacos, G. Poon, et al., “Recent advances with UNSW vanadium-based redox flow batteries,” Int. J. Energy Res., vol. 34, no. 2, pp. 182-189, 2010.

[5] B. Xiong, J. Tang, Y. Li, Z. Wang, C. Xie, X. Zhang, and H. B. Gooi, “Design of a two-stage control strategy of vanadium redox flow battery energy storage systems for grid application,” IEEE Trans. Sustain. Energy, vol. 13, no. 4, pp. 2079-2091, October 2022, doi: 10.1109/TSTE.2022.3181751.

[6] B. Xiong, Y. Yang, J. Tang, Y. Li, Z. Wei, et al., “An enhanced equivalent circuit model of vanadium redox flow battery energy storage systems considering thermal effects,” IEEE Access, vol. 7, pp. 162297-162308, November 2019, doi: 10.1109/ACCESS.2019.2952212.

[7] C. Choi, S. Kim, R. Kim, et al., “A review of vanadium electrolytes for vanadium redox flow batteries,” Renew. Sustain. Energy Rev., vol. 69, pp. 263-274, 2017.

[8] H. Fink and M. Remy, “Shunt currents in vanadium flow batteries: Measurement, modelling and implications for efficiency,” J. Power Sources, vol. 284, pp. 547-553, 2015.

[9] F. T. Wandschneider, S. Röhm, P. Fischer, et al., “A multi-stack simulation of shunt currents in vanadium redox flow batteries,” J Power Sources, vol. 261, pp. 64-74, 2014.

[10] H. W. Chou, F. Z. Chang, H. J. Wei, et al., “Locating shunt currents in a multistack system of all-vanadium redox flow batteries,” ACS Sustain. Chem. Eng., vol. 9, no. 12, pp. 4648-4659, 2021.

[11] Electrochemical energy storage for renewable sources and grid balancing. Newnes, 2014.

[12] M. Skyllas-Kazacos, J. McCann, Y Li, et al., “The mechanism and modelling of shunt current in the vanadium redox flow battery,” ChemistrySelect, vol. 1, no. 10, pp. 2249-2256, 2016.

[13] H. Chen, S. Wang, H Gao, et al. “Analysis and optimization of module layout for multi-stack vanadium flow battery module,” J. Power Sources, vol. 427, pp. 154-164, 2019.

[14] S. König, M. R. Suriyah, T Leibfried, “Model based examination on influence of stack series connection and pipe diameters on efficiency of vanadium redox flow batteries under consideration of shunt currents” [J]. Journal of Power Sources, 2015, 281: 272-284.

[15] A. Tang, J. Bao, and M. Skyllas-Kazacos, “Dynamic modelling of the effects of ion diffusion and side reactions on the capacity loss for vanadium redox flow battery,” J. Power Sources, vol. 196, pp. 10737-10747, 2011.

[16] S. Corcuera and M. Skyllas-Kazacos, “State-of-charge monitoring and electrolyte rebalancing methods for the vanadium redox flow battery,” Eur. Chem. Bull., vol. 1, pp. 511-519, 2012.

[17] Y. Yan, Y. Li, M. Skyllas-Kazacos, et al., “Modelling and simulation of thermal behaviour of

vanadium redox flow battery" [J]. Journal of Power Sources, 2016, 322: 116-128.
[18] A. Tang, J. McCann, J. Bao, et al., "Investigation of the effect of shunt current on battery efficiency and stack temperature in vanadium redox flow battery," J. Power Sources, vol. 242, pp. 349-356, 2013.
[19] C. Yin, S. Guo, H Fang, et al., "Numerical and experimental studies of stack shunt current for vanadium redox flow battery," Appl. Energy, vol. 151, pp. 237-248, 2015.
[20] A. Tang, J. McCann, J. Bao, and M. Skyllas-Kazacos, "Investigation of the effect of shunt current on battery efficiency and stack temperature in vanadium redox flow battery," J. Power Sources, vol. 242, pp. 349-356, Nov. 2013.
[21] X. Yuan, X. Liu, and J. Zuo, "The development of new energy vehicles for a sustainable future: A review," Renew. Sustain. Energy Rev., vol. 42, pp. 298-305, 2015.
[22] L. Chen and Y. Zhang, "Modeling of electric vehicle charging load and its optimal control strategy," in Proc. 33rd Chin. Control Conf., Nanjing, pp. 8210-8215, 2014.
[23] N. Novas, A. Alcayde, I. Robalo, et al., "Energies and its worldwide research," Energies, vol. 13, no. 24, Art. no. 6700, 2020.
[24] R. Li and Z. Hu, "Stochastic optimization strategy for daily operation of electric bus charging station with PV and energy storage," Power Syst. Technol., vol. 41, no. 12, pp. 3772-3780, 2017.
[25] E. S. Díez, E. Ventosa, M. Guarnieri, et al., "Redox flow batteries: Status and perspective towards sustainable stationary energy storage," J. Power Sources, vol. 481, Art. no. 228804, 2021.
[26] V. K. Yu and D. Chen, "Peak power prediction of a vanadium redox flow battery," J. Power Sources, vol. 268, pp. 261-268, 2014.
[27] Z. Wei, S. Meng, K. J. Tseng, et al., "An adaptive model for vanadium redox flow battery and its application for online peak power estimation," J. Power Sources, vol. 344, pp. 195-207, 2017.
[28] B. Xiong, J. Tang, Y. Li, Z. Wang, C. Xie, X. Zhang, and H. B. Gooi, "Design of a two-stage control strategy of vanadium redox flow battery energy storage systems for grid application," IEEE Trans. Sustain. Energy, vol. 13, no. 4, pp. 2079-2091, October 2022
[29] B. Xiong, J. Zhao, K. J. Tseng, M. Skyllas-Kazacos, T. M. Lim, and Y. Zhang, "Thermal hydraulic behavior and efficiency analysis of an all-vanadium redox flow battery," J. Power Sources, vol. 242, pp. 314-324, 2013.
[30] J. D. Gao, L. L. Huang, J. Shen, et al., "Wind and solar energy storage and charging management strategy for smart station area," Zhejiang Electric Power, vol. 39, no. 5, pp. 21-26, 2020.
[31] C. Zou, A. Klintberg, Z. Wei, B. Fridholm, T. Wik, and B. Egardt, "Power capability prediction for lithium-ion batteries using economic nonlinear model predictive control," J. Power Sources, vol. 396, pp. 580-589, August 2018.
[32] M. J. Esfandyari, M. R. H. Yazdi, V. Esfahanian, M. Masih-Tehrani, H. Nehzati, and O. Shekoofa, "A hybrid model predictive and fuzzy logic-based control method for state of power estimation of series-connected Lithium-ion batteries in HEVs," J. Energy Storage, vol. 24, p. 100758, August 2019.
[33] O. I. Olanrewaju and J. M. Maciejowski, "Economic equivalence of economic model predictive control and hierarchical control schemes," Ind. Eng. Chem. Res., vol. 55, no. 41,

pp. 10978–10989, October 2016.
[34] A. Ferramosca, D. Limon, and E. F. Camacho, “Economic MPC for a changing economic criterion for linear systems,” IEEE Trans. Autom. Control., vol. 59, no. 10, pp. 2657–2667, Oct. 2014.
[35] B. Xiong, J. Zhao, and J. Li , “Modeling of an all-vanadium redox flow battery and optimization of flow rates,” in Proc. 2013 IEEE Power Energy Soc. Gen. Meeting, Vancouver, BC, pp. 1–5, 2013.
[36] P. Piya and M. Karimi-Ghartemani, “A stability analysis and efficiency improvement of synchronverter,” in 2016 IEEE Applied Power Electronics Conference and Exposition (APEC), Long Beach, CA, USA, March 2016, pp. 3165–3171.
[37] M. Ren, T. Li, K. Shi, P. Xu, and Y. Sun, “Coordinated control strategy of virtual synchronous generator based on adaptive moment of inertia and virtual impedance,” IEEE J. Emerg. Sel. Topics Circuits Syst., vol. 11, no. 1, pp. 99–110, March 2021.
[38] K. Shi, H. Ye, W. Song, and G. Zhou, “Virtual inertia control strategy in microgrid based on virtual synchronous generator technology,” IEEE Access, vol. 6, pp. 27949–27957, 2018.
[39] P. Xing, X. Jia, C. Tian, Y. Mao, L. Yu, and X. Jiang, “Pre-synchronization control method of virtual synchronous generator with alterable inertia,” in 2019 IEEE 10th International Symposium on Power Electronics for Distributed Generation Systems (PEDG), June 2019, pp. 142–146.
[40] L. Ning, Z. Xiang, C. Yujie, H. Fuxing, Z. Shiqian, and W. Yelin, “Virtual synchronous generator technology and its parallel control strategy in isolated island microgrid,” in 2019 IEEE 10th International Symposium on Power Electronics for Distributed Generation Systems (PEDG), June 2019, pp. 316–320.
[41] K. Shi, H. Ye, W. Song, and G. Zhou, “Virtual inertia control strategy in microgrid based on virtual synchronous generator technology,” IEEE Access, vol. 6, pp. 27949–27957, 2018.
[42] Y. Wei, H. Zhang, Q. Song, and K. Sun, “Control strategy for parallel-operated virtual synchronous generators,” in 2016 IEEE 8th International Power Electronics and Motion Control Conference (IPEMC-ECCE Asia), 2016, pp. 2015–2021.
[43] M. Ebrahimi, S. A. Khajehoddin, and M. Karimi-Ghartemani, “An improved damping method for virtual synchronous machines,” IEEE Trans. Sustain. Energy, vol. 10, no. 3, pp. 1491–1500, July 2019.
[44] Y. Yang, P. Yang, W. Lin, Z. Li, and G. Lu, “A decentralized control for non-error frequency regulation in an islanded microgrid containing multiple VSGs,” International Journal of Electrical Power & Energy Systems, vol. 133, p. 107337, December 2021.
[45] J. Liu, Y. Miura, H. Bevrani, and T. Ise, “Enhanced virtual synchronous generator control for parallel inverters in microgrids,” IEEE Trans. Smart Grid, vol. 8, no. 5, pp. 2268–2277, September 2017.
[46] W. Wu et al., “A virtual inertia control strategy for DC microgrids analogized with virtual synchronous machines,” IEEE Trans. Ind. Electron., vol. 64, no. 7, pp. 6005–6016, July 2017.
[47] J. Alipoor, Y. Miura, and T. Ise, “Distributed generation grid integration using virtual synchronous generator with adoptive virtual inertia,” in 2013 IEEE Energy Conversion Congress and Exposition, Denver, CO, USA, September 2013, pp. 4546–4552.
[48] T. Shintai, Y. Miura, and T. Ise, “Oscillation damping of a distributed generator using a virtual

synchronous generator," IEEE Trans. Power Delivery, vol. 29, no. 2, pp. 668–676, April 2014.

Part C

1. List of Project Publications

The list of the publications achieved in four years of the project are presented in sub-sections below:

1.1 Journal Papers

Year 1: 2019-2020

1. Ujjal Manandhar, Wang Benfei, Zhang Xinan, Gooi Hoay Beng, Liu Yitao, and Abhisek Ukil, “Joint Control of Three-Level DC-DC Converter Interfaced Hybrid Energy Storage System in DC Microgrids,” in IEEE Transactions on Energy Conversion, vol. 34, no. 4, pp. 2248-2257, December 2019, doi: 10.1109/TEC.2019.2935787.
2. Jian Ye and Gooi Hoay Beng, “Phase Angle Control Based Three-Phase DVR with Power Factor Correction at Point of Common Coupling,” in Journal of Modern Power Systems and Clean Energy, vol. 8, no. 1, pp. 179-186, January 2020, doi: 10.35833/MPCE.2018.000428.
3. Wang Benfei, Zhang Xinan, Ujjal Manandhar, Gooi Hoay Beng, Liu Yitao, and Xiaojun Tan, “Bidirectional Three-Level Cascaded Converter with Deadbeat Control for HESS in Solar-Assisted Electric Vehicles,” in IEEE Transactions on Sustainable Energy, vol. 11, no. 4, pp. 2356-2366, October 2020, doi: 10.1109/TSTE.2019.2956054.
4. Benfei Wang, Yu Wang, Yan Xu, Xinan Zhang, Hoay Beng Gooi, Abhisek Ukil and Xiaojun Tan, “Consensus-based Control of Hybrid Energy Storage System with a Cascaded Multiport Converter in DC Microgrids,” in IEEE Transactions on Sustainable Energy, vol. 11, no. 4, pp. 2356-2366, October 2020, doi: 10.1109/TSTE.2019.2956054.

Year 2: 2020-2021

5. Ujjal Manandhar, Zhang Xinan, Gooi Hoay Beng, Wang Benfei and Ye Jian, “Active DC-link Balancing and Voltage Regulation Using Three-Level Converter for Split Link Four-Wire System,” in IET Power Electronics, 13: 2424-2431. https://doi.org/10.1049/iet-pel.2020.0067
6. Feng Fan, Zhang Xin, Zhang Junming, and Gooi Hoay Beng, “Stability Enhancement via Controller Optimization and Impedance Shaping for Dual Active Bridge-Based Energy Storage Systems,” in IEEE Transactions on Industrial Electronics, vol. 68, no. 7, pp. 5863-5874, July 2021, doi: 10.1109/TIE.2020.2992947.
7. Lalitha Subramanian, Vincent Debusschere, Gooi Hoay Beng, and Nouredine Hadjsaid, “A Distributed Model Predictive Control Framework for Grid-friendly Distributed Energy Resources,” in IEEE Transactions on Sustainable Energy, vol.

12, no. 1, pp. 727-738, January 2021, doi: 10.1109/TSTE.2020.3018913.

Year 3: 2021-2022

8. Lalitha Subramanian, Vincent Debusschere, Gooi Hoay Beng, and Nouredine Hadjsaid, “A Cooperative Rate-based Model Predictive Framework for Flexibility Management of DERs,” IEEE Transactions on Energy Conversion, Vol. 36, No. 4, pp. 2724-2733, December 2021.
9. Xiong Binyu, Dong Sidi, Li Yang, Tang Jinrui, Su Yixin, and Gooi Hoay Beng, "Peak Power Estimation of Vanadium Redox Flow Batteries Based on Receding Horizon Control," IEEE Journal of Emerging and Selected Topics in Power Electronics, doi: 10.1109/JESTPE.2022.3152588.
10. Ma Yue, Huang Qi, Gooi Hoay Beng, Zhang Zhenyuan, Yang Xiaomei, and Wang Yang, “Subsynchronous Oscillation Analysis Using Multisynchrosqueezing Transform and Dissipating Energy Flow Method,” in IEEE Transactions on Industry Applications, vol. 58, no. 3, pp. 3134-3141, May-June 2022, doi: 10.1109/TIA.2022.3149684.

Year 4: 2022-2023

11. Xiong Binyu, Tang Jinrui, Li Yang, Wang Zirui, Xie Changjun, Zhang Xinan, and Gooi Hoay Beng, "Design of A Two-Stage Control Strategy of Vanadium Redox Flow Battery Energy Storage Systems for Grid Application," in IEEE Transactions on Sustainable Energy, vol. 13, no. 4, pp. 2079-2091, October 2022, doi: 10.1109/TSTE.2022.3181751.
12. Haifeng Qiu and Hoay Beng Gooi, " A unified MILP solution framework for adaptive robust scheduling problems with mixed-integer recourse objective," in IEEE Transactions on Power Systems, vol. 38, no. 1, pp. 952-955, January 2023, doi: 10.1109/TPWRS.2022.3207067.
13. Haifeng Qiu and Hoay Beng Gooi, " Identifying differential scheduling plans for microgrid operations under diverse uncertainties," in IEEE Transactions on Sustainable Energy, vol. 14, no. 1, pp. 309-324, January 2023, doi: 10.1109/TSTE.2022.3211865.
14. Haifeng Qiu, Qirun Sun, Xi Lu, Hoay Beng Gooi and Suhan Zhang, "Optimality-feasibility-aware multistage unit commitment considering nonanticipative realization of uncertainty," Applied Energy, vol. 327, 120062, December 2022.
15. Huang Hongxu, Li Zhengmao, L P Mohasha I Sampath, Jiawei Yang, Hung Dinh Nguyen, Gooi Hoay Beng, Liang Rui, and Gong Dunwei, "Blockchain-enabled Carbon and Energy Trading for Network-Constrained Coal Mines with Uncertainties," in IEEE Transactions on Sustainable Energy, doi: 10.1109/TSTE.2023.3240203.
16. Qiu Haifeng, Gooi Hoay Beng, Gao Hongjun, Veerapandiyan Veerasamy, and Li Yuanzheng, "Cooperative Power Bidding of Smart Community Grids with an Aggregator-Prosumer-Based Hierarchical Framework," Early Access, IEEE Transactions on Smart Grid.
17. Song Qun, Tan Rui, Ren Chao, Xu Yan, Yang Lou, Wang Jianping and Gooi Hoay

Beng, "On Credibility of Adversarial Examples against Learning-Based Grid Voltage Stability Assessment," in IEEE Transactions on Dependable and Secure Computing, 2022, doi: 10.1109/TDSC.2022.3213012.

18. Zhu Wenchao, Guo Bingxin, Li Yang, Yang Yang, Xie Changjun, Jin Jiashu, and Gooi Hoay Beng, "Uncertainty Quantification of Proton-exchange-membrane Fuel Cells Degradation Prediction based on Bayesian-Gated Recurrent Unit," In Press, eTransportation, Elsevier.
19. Liu Tianqi, Zhang Yuhan, Wang Shunliang, Li Xiaopeng, Gooi Hoay Beng, and Amer M.Y.M. Ghias, "Fault Identification and Fault Location Methods for VSC-HVDC Transmission Lines based on Traveling Waveform Difference," International Journal of Electrical Power and Energy Systems, 108867, Vol. 147, May 2023.
20. Zhang Yuhan, Wang Shunliang, Liu Tianqi, Li Xiaopeng, Gooi Hoay Beng, Amer M.Y.M. Ghias, Xu Ruiting, and Chang Tianyu, "A Backup Protection Scheme for Transmission Lines based on Directional Traveling Wave and Waveform Similarity," International Journal of Electrical Power and Energy Systems, 108864, Vol. 147, May 2023.
21. Shailendra Singh, Vijay Babu P, A K Thakur, S P Singh, and Gooi Hoay Beng, “Profit Maximization in ADN through Voltage Control and DR Management with Networked Community Micro-Grids,” Early Access, Transactions on Industry Applications.

1.2 Conference Papers

Year 1: 2019-2020

1. Ujjal Manandhar, Gooi Hoay Beng, Zhang Xinan, Ye Jian, Wang Benfei and Jack Zhang Xin, "Dynamic Evolution Control for Three-Level DC-DC Converter with Supercapacitor System", *45th Annual Conference of the IEEE Industrial Electronics Society*, 14-17, October 2019, Lisbon, Portugal.

Year 2: 2020-2021

2. Ujjal Manandhar, Zhang Xinan, and Gooi Hoay Beng, "PHIL Study and Stability Analysis of Variable Speed Diesel Generator with Supercapacitor", *IEEE Power & Energy Society General Meeting*, 25-29, July 2021, Washington, DC, USA.

Year 3: 2021-2022

3. Feng Fan, Jiayang Fang, Ujjal Manandhar and Gooi Hoay Beng " Comparision of SPS, DPS and CTPS Modulations with Full Consideration of Stability of DAB Converters with Input LC Filter ", Presented at IEEE ECCE-ASIA 2021, 24-27 May 2021, Singapore.
4. Yang Pengfei, Dong Sidi, Tang Jinrui, Li Yang, Xiong Binyu, and Gooi Hoay Beng, “A Multi-physics Model of Vanadium Redox Flow Battery for Grid Control”, *IEEE Power & Energy Society General Meeting,* July 2022, Denver, Colorado, USA.

Year 4: 2022-2023

5. Feng Xiaoling, Li Yang, Su Fuwen, Xue Fei, Xiong Binyu, Gooi Hoay Beng, "A Multi-Stack Vanadium Redox Flow Battery Model Considering Electrolyte Transfer Delay," 2022 IEEE Sustainable Power and Energy Conference (iSPEC), Perth, Australia, 2022, pp. 1-5, doi: 10.1109/iSPEC54162.2022.10033033.
6. Xue Fei, Li Yang, Tang Jinrui, Feng Xiaoling, Zhang Danhong, Xiong Binyu, "Peak Power Estimation Method of Vanadium Redox Flow Battery for Solar-Battery Powered Electric Vehicle Charging Stations,"2022 IEEE Sustainable Power and Energy Conference (iSPEC), Perth, Australia, 2022, pp. 1-5, doi: 10.1109/iSPEC54162.2022.10032988.
7. Yang Pengfei, Zhang Yu, Su Fuwen, Xiong Binyu, Amer Ghias, and Gooi Hoay Beng, "Microgrid Control Method Based on Virtual Synchronous Machines in Islanded Mode," Accepted for presentation at 8th Asia Conference on Power and Electrical Engineering, ACPEE 14-16 April 2023, Tianjin, China.

2. List of PhD, MSc, FYP and DIP Projects.

The funded research program supports the following PhD, MSc, FYP and DIP projects:

2.1 FYP Projects

Year 1: 2019-2020

1. Study of Power Hardware in the Loop Experiment for the Lithium-ion Battery Testing.
   (*Student Name:* Ang Shangsheng)
2. Development of Dynamic Controller of Flywheels for Frequency Regulation of Microgrids.
   (*Student Name: Wong Yuet Xin*)
3. Operation and Control of Triphase Power Converter System Integrated with Li-ion Battery.
   (*Student Name: Tan Yi Da*)
4. Advanced Power Converter Design for Hybrid AC/DC Microgrids.
   (*Student Name: Su Wuxin*)

Year 2: 2020-2021

5. Stability Improvement of Voltage-Droop Control for Distributed Static Compensators in Weak Grids.
   (*Student Name: Yong Xue Jie*)
6. An Improved Modulation Scheme for Dual Active Bridge Converters.
   (*Student Name: Liam Tian Fu*)

Year 3: 2021-2022

7. Grid-responsive Battery Charging/Discharging Schedules for Multi-objective Optimisation of a Solar Powered Building-transportation System.
   (*Student Name: Lee Noven*)

8. Flexible Demand-Side Management Strategies in Solar Intermittency Mitigation (*Student Name: Tan Wei Ming*)

Year 4: 2021-2022

9. Study on Droop Control Method for Islanded Microgrid Operation. (*Student Name: Chiam Tat Chern*)
10. State of Health Estimation for Lithium-Ion Batteries Based on Data Driven Techniques. (*Student Name: Nigel Zachary Chee*)

3.2 DIP Projects

Year 1: 2019-2020

1. Study of Flywheel and Batteries Configuration and Control for its Integration with the Microgrid. (*Student Names: 1. Jacky Koh, 2. Muhammad Tasnim Bin Taslim, 3. Foo Tze Yee Phoebe, 4. Lai En Han, 5. Khoo Ding Yuan, 6. Chan Hong Sen, and 7. Kanin Sae Tiew*)

Year 4: 2022-2023

2. Real-Time Hybrid Simulation Platform for Microgrid and Renewable Energy Studies. (*Student Names: 1. Goh Wei Wen, 2. Liang Wei Zhi, 3. Ivan Tan Kah Keng, 4. Cindy Tang, 5. Kenneth Khui Yi Cheng, 6. Lim Jun Da, 7. Heng Hong Xun*)
DIP team won champion in DIP competition within the **"Smart and Micro Grids for Integration of Renewable Energy Sources" thematic program**.

3.3 MSc Projects

Year 2: 2020-2021

1. Energy Management of DC Microgrid Based on Photovoltaic Combined with Diesel Generator, Battery and Supercapacitor. (*Student Name: Han Shuting*)
2. Performance Analysis of Photovoltaic/Diesel Generator/Battery System Considering Different Types of Diesel Generators using HOMER. (*Student Name: Ramamoorthy Revathy*)

3.3 PhD Projects

Year 2: 2020-2021

1. Stability Improvement and Control Optimization of Isolated Two-Stage AC-DC-DC Converter Systems (*Student Name: Feng Fan*)

Year 3: 2021-2022

1. Stability Enhancement of Inverter-dominated Power Systems using Virtual Inertia Control
   (*Student Name: Lalitha Subramanian*)

8. Declaration

I declare that the information of the project as described in the above report is true and to the best of my knowledge.

Name / Designation Principal Investigator	**Signature Principal** Investigator	**Date**
Asst Prof Amer M. Y. M Ghias, PI, School of EEE, NTU, SG		15/4/2023

Name / Designation Collaborator(s) (Industry/Institute)	**Signature** Collaborator(s) (Industry/Institute)	**Date**
Dr. GOOI Hoay Beng, Co-PI School of EEE, NTU, SG	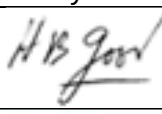	15/4/2023
Dr. Zhang Xinan, Collaborator, School of EEE, UWA, AU		15/4/2023

Name / Designation Director of Research (of the Host Institution)	**Signature** Director of Research (of the Host Institution)	**Date**
Prof FUNG Tat Ching Director,Research Support Office		15 Aug 2023

[Endorsement from host unit has been obtained in RISE with progressReportId=2157]

Organization Stamp: Nanyang Technological University, Singapore

(*Organization's name*)

**Please note that the completeness of the report submitted will help to ensure the efficient processing of the disbursement claim.*